Deep-Sea Research I 99 (2015) 87–104

Contents lists available at ScienceDirect

Deep-Sea Research I

journal homepage: www.elsevier.com/locate/dsri

Internal waves on the upstream side of a large sill of the Mascarene Ridge: a comprehensive view of their generation mechanisms and evolution

J.C.B. da Silva [a,*], M.C. Buijsman [b], J.M. Magalhaes [a]

[a] CIMAR/CIIMAR – Interdisciplinary Centre of Marine and Environmental Research & Department of Geosciences, Environment and Spatial Planning, University of Porto, Rua dos Bragas 289, 4050-123 Porto, Portugal

[b] University of Southern Mississippi, Department of Marine Science, 1020 Balch Blvd, Stennis Space Center, MS 39529, USA

ARTICLE INFO

Article history:
Received 2 May 2014
Received in revised form
23 December 2014
Accepted 7 January 2015
Available online 4 February 2015

Keywords:
Internal solitary waves
Lee waves
Multimodal bore
Local generation
Mode-1 mode-2 internal solitary wave ressonance
Synthetic aperture radar

ABSTRACT

In this paper we aim to clarify the generation of Internal Solitary Waves (ISWs) at work to the east of the Mascarene Plateau (Indian Ocean) using Synthetic Aperture Radar (SAR) imagery and MITgcm fully nonlinear and nonhydrostatic simulations. Realistic representations of stratification and bathymetry are used with asymmetric tidal forcing (including the steady South Equatorial Current which is assumed barotropic in the model) along a 2D transect aligned with the propagation direction of the wave signatures identified in the SAR. The combined flow (i.e. steady and tidal currents) is subcritical with respect to first-mode Internal Waves (IWs), but supercritical with respect to higher wave modes. Different types of nonlinear wave trains with distinct origins (i.e. tidal phase and location) have been identified with the combined aid of model and SAR: (1) large-scale primary mode-1 ISWs evolve from the disintegration of a multimodal baroclinic structure that appears on the upstream side of the sill; (2) mode-2 ISW-like waves that evolve from this same baroclinic structure and are arrested over the sill before being released upstream at the change of flow condition; (3) a large mode-2 lee wave is generated downstream of the sill (i.e. on the west side), which is trapped there during maximum westward tidal flow and released upstream when the tide relaxes; and (4) mode-2 ISW-like waves whose length-scales are O (20 km) appear some 50 km upstream of the sill, after an Internal Tide (IT) beam scatters into the pycnocline, itself originating from critical topography on the leeward (i.e. westward) side of the sill. The underwater sill being investigated is in the mixed-tidal-lee wave regime, where the internal tide release mechanism, lee wave generation and IT beams can coexist. The large-scale mode-2 ISW-like waves that form far upstream from the sill are long-lived features and can be identified in the SAR due to associated short-scale mode-1 ISWs which propagate with the same phase speed, i.e. in resonance. This coupling is also seen in the model, and here it is argued that the formation of those mode-2 ISW-like waves appears to originate from the IT beam after it reflects from the sea surface and interacts with the pycnocline, a generation mechanism referred in the literature as "local generation of ISWs". This IW generation process may be easily overlooked and could be at work in many more regions of the world than previously thought.

1. Introduction

The generation of nonlinear internal waves or Internal Solitary Waves (ISWs) in the ocean is generally recognized as a complex phenomenon that after 40 years of research (see e.g. Lee and Beardsley, 1974; Maxworthy, 1979; Lai et al., 2010) still remains a subject of active investigation. Some of the most common generation mechanisms of ISWs are associated with stratified strong tidal flows over large amplitude sills or submarine ridges, which generate ISWs close to the area of topographic interaction. These Internal Waves (IWs) are usually documented as nonlinear wave trains, internal undular bores, or ISWs, and may arise from the relaxation of internal hydraulic (supercritical) flows (Maxworthy, 1979; Apel et al., 1985; Brandt et al., 1997; Farmer and Armi, 1999a, 1999b), the release of internal lee waves (Haury et al., 1979; Farmer and Smith, 1980), intrusions created by collapsing mixed layers (Maxworthy, 1980), or some form of upstream influence (Baines, 1984; Grimshaw and Smyth, 1986; Melville and Helfrich, 1987; Grue

* Corresponding author. Tel: +351 2204 02476; fax: +351 220402490.
E-mail address: jdasilva@fc.up.pt (J.C.B. da Silva).

http://dx.doi.org/10.1016/j.dsr.2015.01.002

Table 1
Non-dimensional parameters used to characterize tidal flow over bottom topography in the ocean. The densimetric and topographic Froude numbers (Fr and Fr_t, respectively) are given together with the tidal excursion length (δ). U_{max} is a representative value of the maximum flow velocity over the topography (with characteristic width L and height H), c is the phase speed for long linear internal waves (modes-1 and 2), N_{max} is the maximum value for the buoyancy frequency, and ω is the semi-diurnal tidal frequency (M_2).

Study region	$Fr=U_{max}/c$		$Fr_t=N_{max}/U_{max}$	$\delta=U_{max}/L\omega$
	Mode 1	Mode 2		
Mascarene Ridge (near-field)	≈ 0.5	≈ 1.0	≈ 200	≈ 0.1
Luzon Strait After Buijsman et al. (2010) and Ramp et al. (2012)	≈ 0.4	≈ 1.0	≈ 500	≈ 0.04
Knight Inlet After Farmer and Smith (1980)	< 1.0	≈ 2.4	$\approx 1.4–5.0$	$\approx 1–2$

et al., 1997; Cummins et al., 2003; Lai et al., 2010) – just to name a few generation mechanisms, which would clearly benefit from a unifying theory.

A particular issue that has recently regained interest (see e.g. Scotti et al., 2007; Lai et al., 2010) concerns the ambiguity regarding the precise location (i.e either upstream or downstream) and tidal phase of the exact physical feature (i.e. isopycnal perturbations) from which IW trains eventually originate. While Lee and Beardsley (1974), indicated as L.B. in what follows proposed that the IWs are formed on the upstream side of the sill that originates the disturbance, Maxworthy (1979) concluded that the blocking effect of an obstacle on an oncoming stratified tidal flow would only result in a quasi-stationary lee wave on the downstream side of the obstacle, with a phase velocity opposite to the flow direction. This "lee wave" mechanism is based on the theory of supercritical flows, which uses the densimetric (or internal) Froude number (Fr, formally introduced later in Section 3) to characterize the hydraulic state of a stratified flow (i.e. subcritical, critical or supercritical) with regard to the linear long IW phase speed.

It is important to note that in Maxworthy (1979) the flow clearly reached supercritical speeds ($Fr>1$ with regard to all IW modes) during a significant period of the experiment – which may not always be the case. This means that information can only propagate downstream (i.e. in the same direction of the flow), because the fluid velocity is greater than the IW phase speeds. During the accelerating phase of the tidal flow, when the Froude number reached a critical value ($Fr=1$), a disturbance on the interface (downstream of the sill) remains stationary and accumulates energy through resonance. Such a lee wave cannot propagate against the flow in the upstream direction until the relaxation of the tidal stream over the sill, i.e. when its phase velocity exceeds the slackening current. Subsequently, the pycnocline depression advances over the sill's crest and a packet of ISWs is formed. The model proposed by Maxworthy (1979) successfully explained the generation of nonlinear IW trains in various regions of the world's oceans (see e.g., Apel et al., 1985 and Brandt et al., 1997).

Subsequent studies concluded that both L.B. and Maxworthy's (1979) mechanisms could apply depending on the flow criticality (see e.g. Haury et al., 1979; Farmer and Smith, 1980; Chereskin, 1983; Matsuura and Hibiya, 1990), although they have never been found simultaneously at work. We note however that the flow may be subcritical with respect to the fundamental mode but supercritical with respect to higher modes (e.g. mode-2). In this case, as reported by Farmer and Smith (1980), a mode-2 lee wave is formed downstream while at the same time, mode-1 ISWs are also formed upstream of the sill's crest, in what appears to be an independent process. In this last case mode-1 ISW generation has been explained in terms of partial blocking and upstream influence, which is identified in state-of-the-art numerical models as the mechanism responsible for ISW generation upstream of several ocean sills (e.g. Cummins et al., 2003; Scotti et al., 2007; Stashchuk and Vlasenko, 2007; Lai et al.; 2010; Buijsman et al. 2010), even when the flow is supercritical (with regard to all modes) over the sill's crest.

Another example of upstream influence has also been identified in the South China Sea (SCS) by Buijsman et al. (2010) who termed "internal tide release mechanism" to the generation of large amplitude ISWs from the asymmetrical flow across a large ridge (including tidal and steady currents). In this case, strong currents lift the isopycnals higher upstream of the ridge (i.e. creating an elevation wave there), allowing for a large energy density to accumulate on this side. As soon as the current slackens, this elevation wave is released upstream and ISWs form on its back slope – see Buijsman et al. (2010) for further details.

IW beams generated at critical slopes (i.e. where beam and bottom slopes match together) may also generate ISWs by means of an altogether different mechanism, termed "local generation" (New and Pingree, 1992). These ISWs are not directly related to topography, but are generated by an internal tidal beam hitting the seasonal thermocline at an oblique angle. The internal tide beam interacts with the interface and creates an interfacial wave there, which may then evolve through nonlinear steepening into ISWs (see e.g. New and Pingree, 1990, 1992; Gerkema, 2001; Akylas et al., 2007; Grisouard and Staquet, 2010; Mercier et al., 2012; Dossmann et al. 2013). Satellite imagery has confirmed the effectiveness of this generation mechanism in the Bay of Biscay (New and da Silva, 2002; Azevedo et al., 2006) as well as in other locations, such as off Portugal (da Silva et al., 2007) and in the Mozambique Channel (da Silva et al., 2009). Particularly relevant for the present study, is the work of Grisouard et al. (2011), which discusses the local generation of ISWs with a higher mode vertical structure (e.g. modes-2 and 3) in the vicinity of the beam impact. Their findings are tested in this paper to account for the generation of mode-2 ISW-like waves observed upstream of the sill, in the Mascarene Ridge region. We will also demonstrate that these ISWs are relatively long-lived, contrasting with other observations of mode-2 ISW-like waves previously reported (e.g. those in Shroyer et al., 2010, which have lifetimes of typically less than a few hours).

A particular scenario where lee waves, upstream influence and tidal beams can coexist is of key importance to our study. This generation scenario has already been discussed in the parameter space given in Garrett and Kunze (2007) (see their region 4), or alternatively in the mixed tidal lee wave regime discussed in Nakamura et al. (2000). The topographic Froude number (Fr_t) and the normalized tidal excursion length (δ), defined as: $Fr_t = N_{max}H/Uo$ and $\delta = Uo/L\omega$ (see also Table 1), are set as two major parameters governing the different generation regimes for IWs. In particular, a large Fr_t and a small δ mean that significant blocking effects (owing to bathymetry) will simultaneously allow for upstream influence and lee waves to develop upstream and downstream of the obstacle (see Garrett and Kunze, 2007; Klymak et al., 2010), while still allowing tidal beams to develop in the presence of critical slopes (see Nakamura et al., 2000). Figure 4 of Buijsman et al. (2010) exemplifies precisely that, since a lee wave forms downstream of the sill together with an internal tidal beam whose energy propagates upstream and towards the surface (i.e. an upstream-leaning beam). The authors further note that, similar upstream-leaning beams have also been

shown in model studies of oscillating flow over a ridge by Morozov and Vlasenko (1996), Nakamura et al. (2000), Kanarska et al. (2007), Legg and Klymak (2008), Shaw et al. (2009), and Dossmann et al. (2013).

In this paper we re-examine the image dataset used in da Silva et al. (2011) and New et al. (2013) and add a modelling perspective to their previous work seeking further knowledge about the detailed generation mechanisms responsible for mode-1 and mode-2 ISW-like waves to the east of the Mascarene Plateau. The results of a fully nonlinear and non-hydrostatic numerical model are analysed aiming to identify the exact tidal phase and location of these "nascent" IWs. While Konyaev et al. (1995) and da Silva et al. (2011) reported that mode-2 short-period IWs are generated by the lee wave on the downstream (i.e. westward) side of the sill during maximum westward flow, da Silva et al. (2011) proposed that the large mode-1 ISWs observed to the east of the sill could also result from this large tidally generated depression of the upper thermocline. However, da Silva et al. (2011) based their interpretation on a travel–time graph reconstructed from a limited set of SAR images and linear best fits to the data points in a time vs. space coordinate system. Despite this being usual practice (see e.g. New et al., 2013 and da Silva and Helfrich, 2008), two particularities may introduce misleading errors in the deduced origin (in time and space) for the waves: (1) sampling restrictions due to the sun-synchronous satellite orbit (within the flood–ebb cycle) results in aliasing, so that near spring tides (when the IWs are observed) the images always correspond to a similar flood–ebb phase of the semi-diurnal tide (see e.g. Valente and da Silva, 2009; Mendes et al., 2014); (2) da Silva et al. (2011) neglected IW phase speed variations across shallow bathymetry, which may introduce non-negligible bias from true ISW trajectories in the travel–time graphs.

The remainder of this paper is organized as follows. In Section 2 we present the methodology details concerning the SAR observations and our model settings. In Section 3 we present model results and analyse the densimetric Froude number for wave features identified in the model. The different ISW origins and propagation characteristics are documented and compared with SAR image data in travel–time graphs, considering IW phase speed variations across variable bathymetry. In particular, we seek for evidence of the formation phase of mode-1 and mode-2 ISW-like waves. In Section 4 we analyse the results and propose generation mechanisms of the waves presented in Section 3, and we further inspect the formation of lee waves and discuss their propagation across the sill. A summary and some concluding remarks are presented in the final Section of the paper.

2. Methodology

To assess the generation position and time of the ISWs, and their propagation speeds, da Silva et al. (2011) and New et al. (2013) presented travel–time graphs relating position (distance from a reference point on the west side of the sill – 12.883°S and 60.733°E) and time (with respect to maximum eastward barotropic tidal flow) of each leading ISW within a given packet detected in the SAR images (see e.g. Figure 5 in da Silva et al., 2011). In what

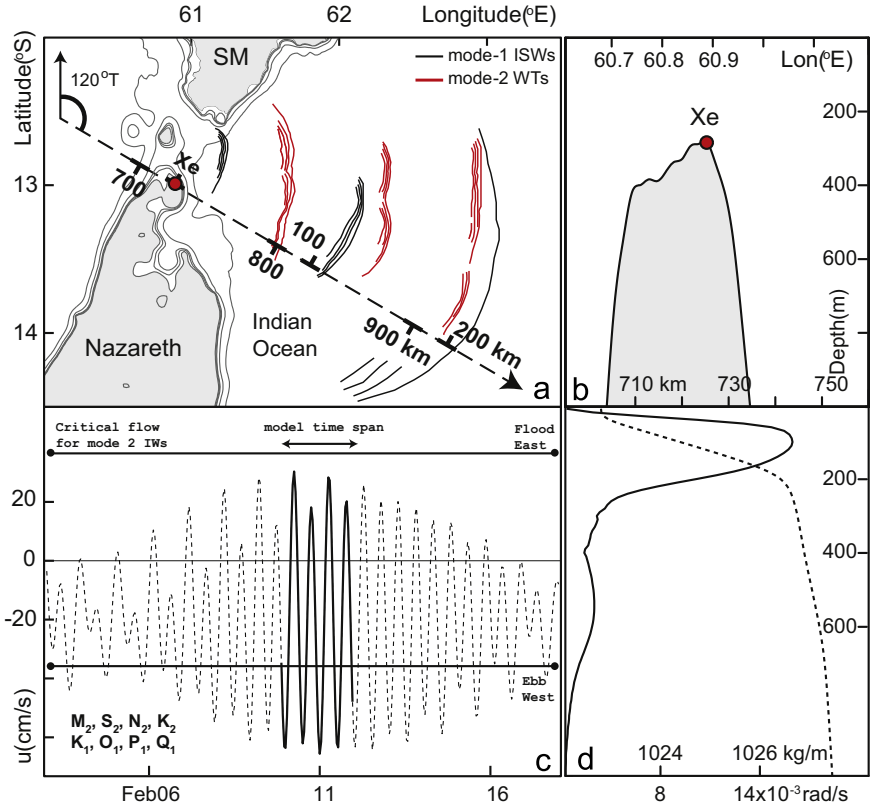

Fig. 1. (a) The Mascarene Ridge region (Indian Ocean) to the east of two major underwater banks: Saya de Malha (SM) and Nazareth. Grey areas represent depths less than 300 m. Additional isobaths for 400, 500, 1000 and 2000 m are shown as solid dark lines. Typical mode-1 (in black) and "wave-tails" (WTs in red) ISWs are shown propagating along 120°T. The MITgcm transect is shown as a dashed black line, and reference distances are shown below it (model coordinates) and above it (distance from Xe). (b) Bathymetry profile for the upper sill section of the model transect where the summit is labelled Xe and marked with a red circle. (c) Tidal flow including a stationary current (SEC) computed at Xe for approximately a fortnight (tidal) period using the tidal constituents indicated on the bottom left corner (model time-span in solid black curve). Thicker horizontal lines indicate the critical regime for mode-2 IWs computed at Xe. (d) Vertical density (dashed line) and buoyancy frequency (solid line) distributions typical of the upstream side of Mascarene Ridge. (For interpretation of the references to color in this figure legend, the reader is referred to the web version of this article.)

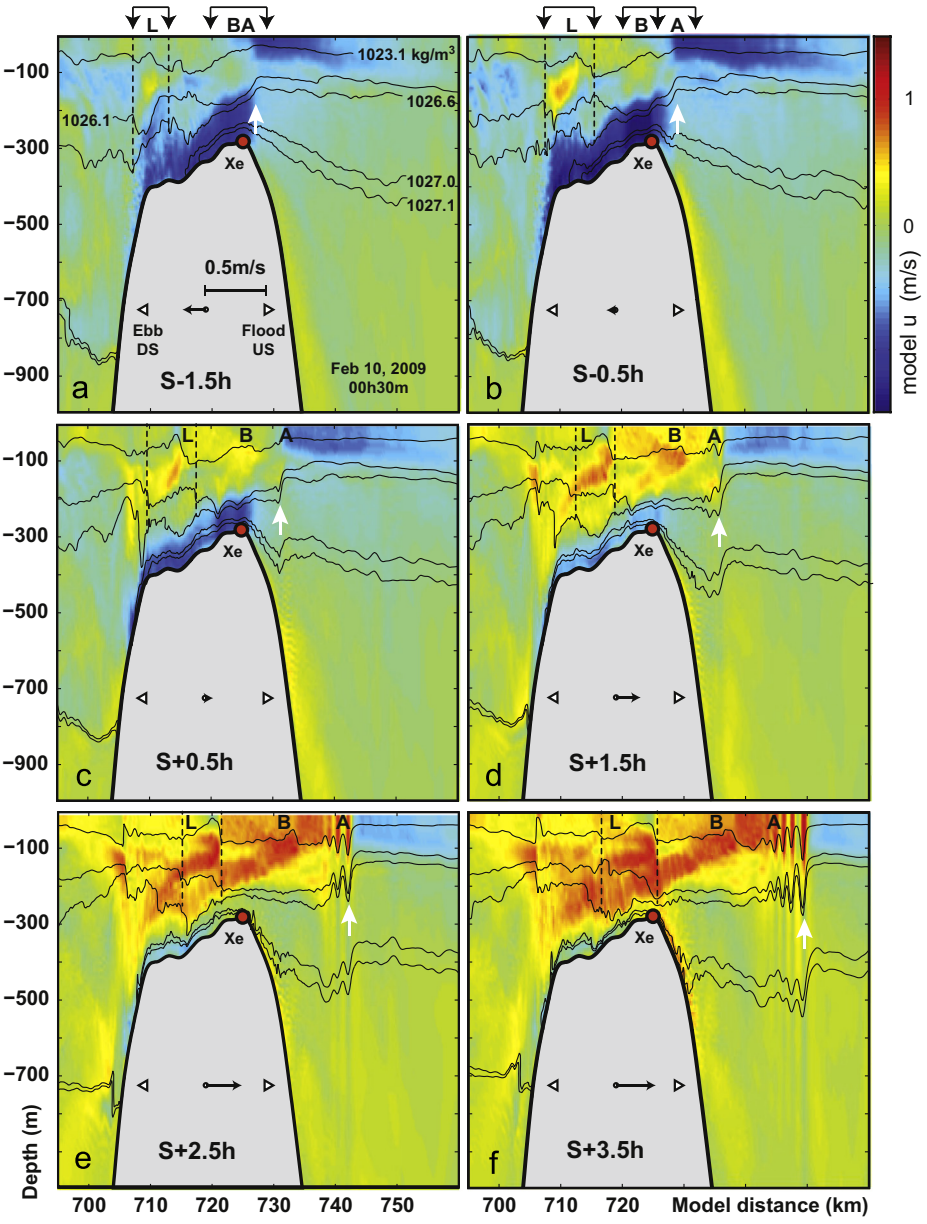

Fig. 2. Model vertical sections of horizontal velocities (u component), shown for a time sequence of 5 h for experiment (ii) – see text for details. Tidal flow and corresponding times for each panel are indicated with respect to slack (S) tide. Selected isopycnals are overlaid in each panel for reference, together with the ebb-ward (i.e. downstream, DS) and flood-ward (i.e. upstream, US) tidal flow. Reference locations tracking the evolution of a lee wave (L) are marked with vertical dashed lines. A mode-2 bulge (B) and mode-1 internal wave (A) are also shown on top of each panel (see text for details). A white arrow is also used to follow a density front disintegrating into a packet of mode-1 ISWs.

follows we use the same methodology combining wave fronts in the SAR with positions identified in the model. We seek to compare the SAR data with the model data, and establish the consistency of the model to predict ISW evolution. In addition, by doing this procedure we should be able to back-trace the ISWs to their point of origin, and assess with accuracy the location and tidal phase of their formation.

2.1. SAR image data

In all, 140 ENVISAT-ASAR images (in Wide Swath mode, WS, with a viewing area of 400×400 km^2) were available and processed from the study region (including an extended dataset requested since 2011 comprising 32 new images that were unavailable to da Silva et al. 2011). In addition, 24 TerraSAR-X images have been analysed, some of which in tandem mode with the ENVISAT (i.e. pairs of image acquisitions approximately 4 h apart). While the ENVISAT (WS) images are ideal to understand the full two-dimensional spatial structure of the ISWs (see e.g. the map in Fig. 1 based on SAR), tandem mode pairs of scenes (TerraSAR-X and ENVISAT) provide insight into the generation mechanisms (see e.g. Fig. 7).

When analysing SAR imagery it is important to recall that, to first order the modulation of short-scale sea surface roughness by variable surface currents is proportional to the surface current gradient along the radar look direction ($\partial u/\partial x$) (see Alpers, 1985), where x is the coordinate in the radar view direction projected onto the horizontal plane. In the framework of weak hydrodynamic interaction together with radar Bragg scattering theory, one can relate spectral values of the ocean surface waves to the Normalized Radar Cross Section (NRCS) by using the following equation:

$$\frac{\delta\sigma}{\sigma_0} = -A\frac{\partial u}{\partial x} \tag{1}$$

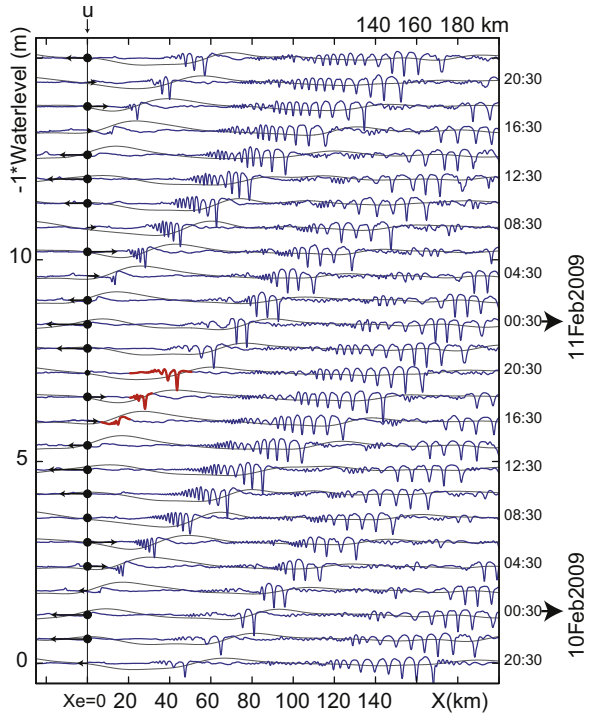

Fig. 3. Hovmöller diagram presenting the displaced water level along the model transect shown in Fig. 1, with time increasing vertically upwards. The black horizontal arrows at Xe correspond to the strength of the barotropic flow (SEC+tide). Long and short-wavelength signals are plotted as grey and blue solid lines, respectively (see text for details). The long-wavelength signal was obtained from a 5th order Butterworth filter with a cut-off of 30 km. Short-wavelength curves highlighted in red represent key segments discussed in the text, and identify mode-1 ISW generation on the upstream side of Xe. (For interpretation of the references to color in this figure legend, the reader is referred to the web version of this article.)

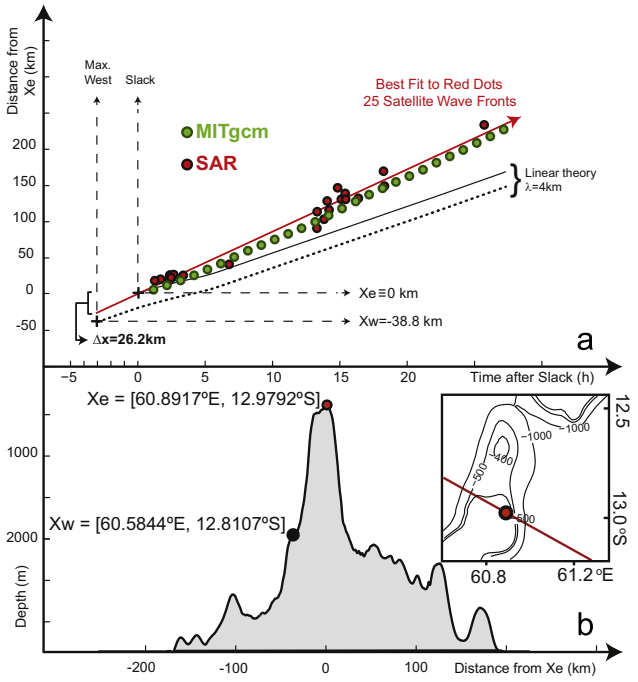

Fig. 4. Upper panel presents a travel–time plot of 25 SAR mode-1 ISW observations (red circles), and corresponding observations taken from the MITgcm (every hour, green circles). A linear fit to the SAR observations (red solid line) is shown together with linear predicted trajectories, assuming generation either at Xe during slack (in solid black) or Xw during maximum westward flow (in dotted black). The bathymetry profile along the waves' propagation path is shown in the bottom panel (see Xe and Xw for reference, shown as red and black circles, respectively) together with the corresponding geographic inset. (For interpretation of the references to color in this figure legend, the reader is referred to the web version of this article.)

where σ denotes the total NRCS ($\delta\sigma = \sigma - \sigma_0$), σ_0 is the NRCS of the background (unaffected by IWs), and A is a constant that depends on wind wave relaxation rate, radar wavelength, polarization and incidence angle. Eq. (1) is an approximation since there are many other factors affecting the radar imaging of IWs (see e.g. da Silva et al., 2000 and Kudryavtsev et al., 2005), but it can be used as a qualitative approximation for the SAR signature of IWs when departures from the radar background, σ_0, are somewhat symmetrical (positive and negative variations relative to a radar mean background clutter), as it is the case for many of the IWs in question. The vertical mode structure of ISW-like waves may also be detected from SAR based on the signature polarity (for more details see e.g. Mercier et al., 2012 or Jackson et al., 2012).

2.2. Numerical model

We apply the fully nonlinear and non-hydrostatic Massachusetts Institute of Technology general circulation model (MITgcm, Marshall et al., 1997) in a 2D (independent of 'y' coordinate) setup with realistic bathymetry of the Mascarene Plateau. The model computes vertical viscosities and diffusivities by Thorpe-sorting unstable density profiles (see Thorpe, 1977) using the subgrid scale dissipation and mixing scheme by Klymak and Legg (2010). Unstable density inversions or overturns may occur in lee waves or hydraulic jumps at steep ridge crests. The scheme finds the maximum overturn length scale and from that it computes a dissipation rate, which is translated into a diffusivity using the Osborn (1980) relation. The diffusivity can have any value (see formulas 2 and 3 in Klymak and Legg, 2010). The density profile is not altered by the scheme. The scheme only returns the viscosities and diffusivities larger than their background values to the model. The unperturbed (i.e. background) vertical diffusivity of temperature for the Mascarene Ridge is assumed $K_{zT}=10^{-5}$ m^2/s according to Lozovatsky et al. (2003) (see their Figure 14 for vertical diffusivities 1000 km from the ridge) and the horizontal diffusivity $K_{HT}=10^{-4}$ m^2/s. These background values were chosen to prevent model instabilities. We assume a Prandtl number of 1, so $A_{vz}=K_{zT}$. The background vertical and horizontal viscosities are $A_{vz}=10^{-5}$ m^2/s and $A_{vH}=10^{-2}$ m^2/s, respectively. A comparable model set up was used in Buijsman et al. (2012).

The total horizontal length of the computational domain is about 1500 km long and comprises 3000 grid cells. The central part of this domain of 500 km, centred at the sill's summit (position Xe at 60.8917°E and 12.9792°S in Fig. 1) is composed of 2500 cells with a size of 200 m. Away from the central high resolution part of the domain, i.e. towards the boundaries, the grid cells are linearly stretched (i.e. telescoped) to 6.3 km. The orientation of the model 2D section thus extends about 750 km to the west and 750 km to the east of position Xe, with an orientation close to the propagation axis of the observed ISWs reported in da Silva et al. (2011), that is towards about 120°T (true North) on the east side of the ridge and on the west side towards about 300°T. The horizontal grid step was chosen to resolve the model's most relevant features (i.e. the IW oscillations ranging from the IT to smaller ISW-like waves including lee waves), without increasing the computational times significantly (e.g. when going to 100 m). Note that this choice for the horizontal grid step is consistent with standard resolution requirements in nonhydrostatic IW modelling (see also Vitousek and Fringer, 2011 and Scotti and Mitran, 2008), since typical thermocline depths in the upstream side of the Mascarene ridge yield leptic ratios of approximately 0.5. This means that the numerical dispersion implicit in the model is in fact smaller than the corresponding physical dispersion, allowing for a better simulation of the actual nonhydrostatic effects.

The model features 120 layers in the vertical. The top 1000 m has cells with a vertical grid spacing of 10 m. Below this layer the

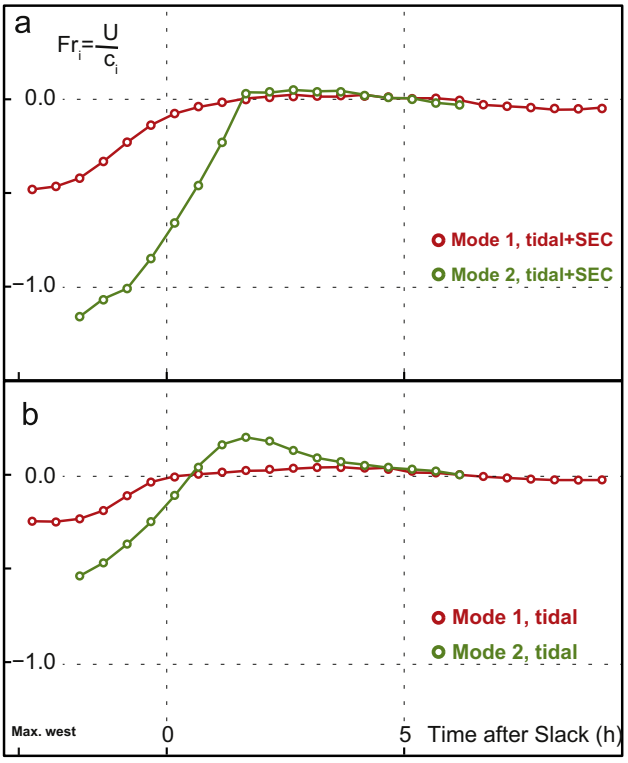

Fig. 5. (a) Froude number every 30 min assuming tidal currents and SEC, calculated along the waves' positions recorded in the model during their early stages of formation (red for mode-1 and green for mode-2). (b) For comparison, similar to (a) but for results considering tidal currents only. (For interpretation of the references to color in this figure legend, the reader is referred to the web version of this article.)

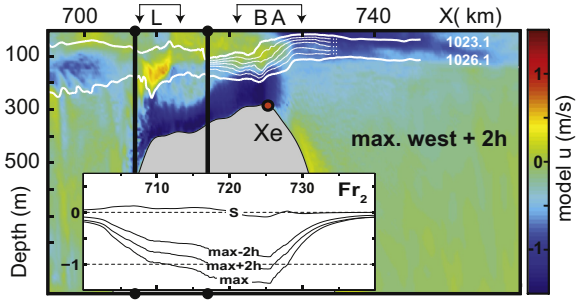

Fig. 6. Modelled horizontal velocities approximately 2 h after maximum westward flow, highlighting a mode-2 lee wave (L), and a multimodal structure (BA, where a series of isopycnals have been overlaid in white). The inset shows a sequence of Froude numbers (Fr_2) computed over the sill as a function of model distance (between 700 and 740 km) for mode-2 IWs. The sequence includes slack water (S), 2 h before maximum westward flow (max-2 h), maximum westward flow (max), and 2 h after maximum westward flow (max+2 h).

model's vertical resolution is stretched to the bottom where it is approximately 50 m. The model uses realistic topography merged from the Smith and Sandwell (1997) database with a resolution of 1 min and high-resolution ship depth soundings collected during R.R.S Charles Darwin cruise 141 and discussed in New et al. (2007). Away from the ridge the model depth is a constant 4000 m (see Fig. 4b). The density stratification was taken directly from conductivity–temperature–depth (CTD) measurements conducted during R.R.S Charles Darwin cruise 141 and was considered being only a function of depth. A typical buoyancy frequency profile $N^2(z) = -g/\rho(d\rho/dz)$ of the upstream side of the ridge (g is the acceleration due to gravity and ρ is the density) is shown in Fig. 1d.

The model forcing is based on tides retrieved from the Ocean Topography Experiment (TOPEX)/Poseidon 7.2 (TPXO7.2) tidal inversion model (Egbert and Erofeeva, 2002). Amplitudes and phases were

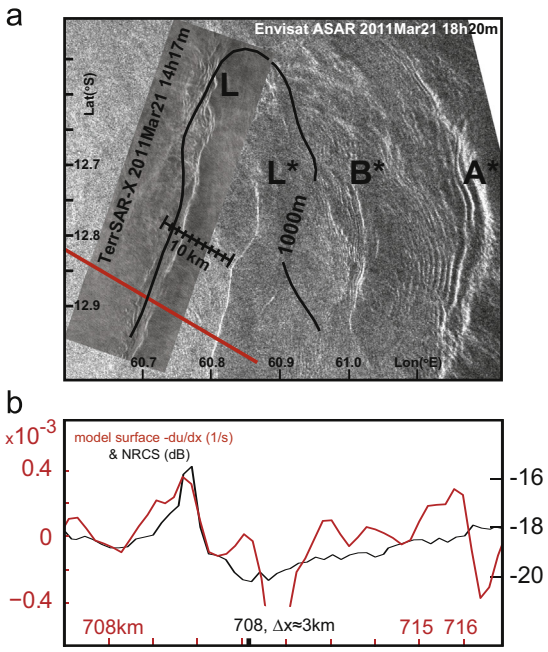

Fig. 7. (a) Composite with two SAR images (4 h apart) showing the evolution of a lee wave surface signature captured with an Envisat-ASAR image (labelled L* in the larger frame), and a TerraSAR-X image (labelled L in the smaller frame with the leading wave centred approximately at 60.75°E and 12.80°S). For reference, the locations of mode-1 (A*) and mode-2 (B*) ISWs corresponding to the near-field evolution of features A and B identified in Fig. 6, are also shown. The 1000 m isobath is shown to highlight the sill (model transect in red). An additional 10 km scale taken across the lee wave structure is also indicated (black ticked line). (b) Black line refers to the TerraSAR-X backscattered NRCS along the wave transect defined in part (a) (i.e. black ticked line), while red line shows the modelled surface velocity gradient (note respective labels for coordinates) corresponding to Fig. 6 between vertical black lines. (For interpretation of the references to color in this figure legend, the reader is referred to the web version of this article.)

extracted from this model at a location (60.7300°E 12.8900°S) just west of the ridge in 1100 m water depth at the same latitude as the 2D transect and scaled to the deep water boundaries of the 2D model. The period of the tidal forcing corresponds to spring tides near 11 February 2009 when large ISWs were observed in the SAR imagery (Figure 2 in da Silva et al., 2011). All model results used in this paper comprise the period indicated in bold in Fig. 1c. Since we are comparing the model with realistic times of SAR, the model was forced with a sufficient amount of tidal constituents to reconstruct realistic forcing, of which the M_2, S_2 and K_1 are the most important (in total 8 constituents with the M_2, S_2, N_2, K_1, K_2, O_1, P_1 and Q_1 tidal frequencies were used). In fact, the M_2 and S_2 constituents are needed to mimic the spring-neap cycle and a further diurnal constituent helps to tune in the magnitude of the tidal beating at the ridge (see Fig. 1c). Note also that, these mixed constituents do not change the semi-diurnal nature of the flood and ebb cycle, which dictates all our time references when comparing the model with the SAR (see below).

Because a steady SEC current has been shown to affect ISW propagation considerably in the study region (see da Silva et al., 2011), we conducted two series of numerical experiments: (i) In the first experiment, only tidal currents were set into the model (i.e. symmetric currents corresponding to the period in Fig. 1c) and (ii) the second experiment was initialized by the same spring intensity of tidal forcing as for (i) and with an additional stationary current whose value is 0.2 m/s at Xe (i.e. corresponding to the SEC at the summit of the sill where depth is 281.3 m). This means that a superposed constant barotropic flow adds a non-tidal component to the forcing. This constant barotropic flow is based on ADCP measurements described in New et al. (2007) which in reality exhibit some shear (see also da Silva et al., 2011). In more detail, we calculated a mean vertical profile

Table 2
Summary of modelled observed properties for mode-1 ISWs propagating upstream of the Mascarene Ridge according to time (after slack tide, transition from westward to eastward flow) and distance travelled from Xe. The maximum registered amplitudes (η) and corresponding depth levels are given together with the leading ISW characteristic width (L) and phase speed (Cp), number of ISWs per packet (n), inter-ISW distance (between first and second ISWs in a given packet), and the horizontal surface velocity registered directly over the trough of the leading ISW.

Time after Slack (h)	Distance to Xe (km)	Max. η (m) and depth level (m)	L (m)	n	Inter-ISW distance (m)	Cp (m/s)	Surface u (m/s)
2.4	17	70 at $z=-125$	800	2–3	1600	1.89	1.0
4.9	36	150 at $z=-145$	1400	7–8	2600	2.45	1.6
9.9	80	200 at $z=-155$	2400	6–7	4800	2.45	1.9
14.9	129	200 at $z=-255$	4200	8–9	7400	2.77	2.0

of u (horizontal velocity component) for a complete (semidiurnal) tidal cycle at station 37 of New et al. (2007), located at 61.27°E, −13.00°N, just to the east of the sill. Then we assumed the calculated magnitude of the depth-averaged current as our barotropic current at that depth (i.e. a barotropic SEC), and impose in the model a steady flux of 56.26 m^2/s to simulate the real SEC. The effect of the barotropic SEC in the generation of ISWs is discussed in Section 3.3. Pursuing a baroclinic (thus more realistic) SEC would have been much more difficult in a 2D model, especially when the sheared flow interacts with the sill. We believe however that our barotropic approximation of the SEC is sufficient to understand the dynamics of ISW generation and their evolution in time, since the results will be shown to agree with the SAR in Section 3. Currents (both tidal and steady SEC) were exponentially ramped from zero to full strength within 24 h to minimize the generation of any unwanted waves.

All forcing was applied at the boundaries, 750 km away from the ridge, with a barotropic flow that is in phase at both west and east boundaries causing a standing barotropic wave. Hence, the depth-integrated horizontal flow is independent of the horizontal coordinate. Since the TPXO amplitudes and phases were extracted close to the ridge, the barotropic velocities in this standing wave best resemble the barotropic velocities at the ridge crest. It would have been more difficult to obtain the correct velocities at the ridge if a progressive tidal wave was applied. Internal wave reflections at the horizontal boundaries were greatly reduced using a sponge, or nudging layer. The velocities and temperature are quadratically nudged over 100 cells near the east and west boundaries to the barotropic horizontal velocities and a time-invariant vertical temperature profile, respectively (see Lavelle and Thacker, 2008). The nudging time scales at the outer boundaries of the nudging layers are 7200 s, increasing quadratically with cell distance towards the inner boundary of the nudging layer. The length of these nudging layers is about 388 km, i.e. greater than one first-mode internal wavelength.

We also refer the interested reader to Appendix A for a brief discussion of the barotropic to baroclinic conversion, fluxes, and dissipation.

3. Results

We start our analysis including both tidal forcing and an additional stationary current tuned to simulate the SEC, as these are the usual environmental conditions in the study region (see Sections 3.1 and 3.2). Then, in Section 3.3, we will study the sensitivity of the model results to the SEC by comparing the two numerical experiments: when only tidal currents were applied in the model (first numerical experiment) with the model results of the second numerical experiment (i.e. steady SEC plus symmetric tide).

3.1. Generation of internal waves in the near field

3.1.1. Multimodal structure over the eastern part of the ridge

In what follows all ISW time records are referred to the tidal phase when the tidal currents reach a relative minimum during the semi-diurnal flood–ebb cycle, i.e. the time reference is a preceding minimum of this cycle, obtained from the OTPS velocity time series using the tidal constituents referred in Section 2.2. We focus on a temporal sequence of model results (with horizontal velocity and some overlaid isopycnals) beginning soon after the maximum westward tidal streaming, looking for the earliest evidence of mode-1 ISWs (see Fig. 2). The model shows that starting from the ebb tide (about 1.5 h before slack tide, i.e. transition from westward to eastward flow), a density front gradually forms over the eastern crest of the sill (i.e. close to the 300 m isobath, above Xe), as it can be seen in the 2nd and 3rd uppermost isopycnals in Fig. 2a (see white vertical arrow in Fig. 2a for location). This density front grows and becomes increasingly steeper (see arrows in parts b and c in Fig. 2) and then starts moving upstream (i.e. eastwards) as soon as the tidal flow relaxes further (Fig. 2 parts c and d). By the time the tidal flow has clearly reversed (i.e. from westward to eastward), the first mode-1 waveforms can be identified to form on the rear slope of the aforementioned density front (see white arrows in Fig. 2 parts d and e). This process takes approximately 2 to 3 h, after which 2–3 ISWs can be identified in the upper isopycnals as well as in the velocity field (see arrow in Fig. 2e). When the tidal flow is close to its maximum flood-ward (i.e. eastwards) an IW train with at least 4 ISWs is clearly identified (see arrow in Fig. 2f). These are clearly mode-1 ISWs as all isopycnal displacements are vertically in phase.

The spatial structure of the mode-1 ISWs observed in the model and in the SAR is well seen when we plot a Hovmöller diagram like that in Fig. 3. The plot displays the modelled water level every two hours (time running vertically upwards) around the period 10–12 February, 2009, as a function of distance from a reference position (Xe, see Figs. 1 and 2). The inter-ISW distances of O(5–10) km and their amplitudes of O(100) m are similar to the ISWs observed by Konyaev et al. (1995) and da Silva et al. (2011) at the Mascarene Plateau (see also Table 2). The inter-packet separation between two consecutive mode-1 wave trains is of about 115 km (see Fig. 3; 10 February 2009 from 16:30 to 20:30 UTC), which translates into an average propagation speed of 2.57 m/s. This is somewhat above (some 30%) the linear wave speed (1.8 m/s) for nonhydrostatic short-IWs with wavelength $\lambda=4$ km in deep water, consistent with the nonlinear character of the ISWs. We also note that the ISW signals corresponding to the period between 16:30 and 20:30 on 10 February 2009 (marked in red thicker lines, Fig. 3) coincide with an elevated long wave (with mode-1 wavelength, in grey) to the east of the ridge (i.e. to the right of Xe in Fig. 3), which develops during and immediately after maximum westward flow. As this elevated long mode-1 wave relaxes to its rest position, a front develops (sharp depression in the short wavelength signal at 16:30 and $X\approx 15$ km, in red) and the backside of the long wave disperses into ISWs (seen e.g. at 20:30 and $X\approx 40$–45 km). A similar long (with mode-1 wavelength) elevation wave has been identified in the SCS as an important feature in the ISW formation process, which is connected to the "internal tide release" generation mechanism proposed in Buijsman et al. (2010). The long waves with mode-1 wavelengths, which were obtained from spatially low-pass filtering the surface elevation signal output from the model, correspond to the mode-1 internal tide.

Using the methodology described in Section 2 we combine 25 wave fronts in the SAR with 27 positions of the leading (mode-1) ISWs from the model (i.e. data taken every hour) in a travel–time graph relating position (distance from Xe) and time (with respect to slack tide). Fig. 4a presents these combined results where red (filled) circles and the red linear fit to those points represent the SAR data, while the green (filled) circles refer to the model results and show the space versus time evolution of the leading (mode-1) ISW in a given wave packet. Note that both model and SAR data comprise more than 25 h, confirming the longevity of these mode-1 ISWs, which propagate during that period for approximately 250 km to the east of the sill. One can see that the SAR and model data are aligned with each other, while the clustering of the SAR data points is due to the orbit characteristics (as mentioned earlier, the orbit is phase locked with the fortnightly spring-neap cycles, meaning that sampling within the flood–ebb cycle is aliased so that near spring tides the images always correspond to a similar flood–ebb phase of the semi-diurnal tide). The best linear fit through the SAR data points (red line in Fig. 4a) intersects the origin of a frame of reference centred at position Xe (60.8917°E, 12.9792°S; see Fig. 4b) and slack tide (transition from westward to eastward tidal flow). This is certainly a possible generation coordinate for the mode-1 ISW trains reported above. However, according to the satellite data another possibility would be 26.2 km downstream (i.e. to west) of position Xe (see Fig. 4a and b), on the lee side of the sill at the time of maximum westward flow, as originally proposed in da Silva et al. (2011) and New et al. (2013).

Before we proceed, note two other curves in Fig. 4a which correspond to the trajectories predicted by linear theory (assuming a characteristic wavelength of approximately 4 km, i.e. nonhydrostatic short-waves, taken directly from the model). These correspond to two possible origins of the mode-1 ISWs: those generated at Xe (i.e. over the crest on the upstream side of the sill) at the time of slack tide (black line in Fig. 4a), and ISWs generated at Xw at the time of maximum westward tidal flow (dark-dotted line in Fig. 4a). As expected from nonlinear theory, the slope of the fit to the data (model fit not shown) is slightly steeper than the slopes predicted from linear theory, which is a consequence of the nonlinear wave speeds of the ISWs being slightly higher than linear theory predicts. Note that the dark-dotted trajectory with origin at Xw at the time of maximum westward flow is always significantly offset from the data points (both SAR and model), which suggests that the "lee wave" generation mechanism postulated in da Silva et al. (2011) and New et al. (2013) may not be operative for the mode-1 ISWs that propagate upstream of the sill. Given this potential ambiguity between the SAR and model suggested origin for the ISWs, i.e. the "lee wave" and the "upstream influence" generation mechanisms, we next examine the criticality of the flow over the sill near the time of wave formation.

The qualitative difference between "lee wave" and "upstream influence" mechanisms, i.e. "arrested and released" versus "evolutionary" mechanisms (see Vlasenko et al., 2013), can be explained quantitatively in terms of a densimetric Froude number analysis. The Froude number was calculated as follows:

$$Fr_i = \frac{U}{c_i} \tag{2}$$

where U is the velocity of the flow (i.e. barotropic tides described in Section 2.2 plus barotropic SEC) along the propagation direction chosen for the section of the 2D model, and c_i is the phase speed of the first or second mode ($i=1, 2$) obtained from a standard Boundary Value Problem (BVP, or Taylor–Goldstein equation with appropriate boundary conditions in its nonhydrostatic formulation):

$$\frac{d^2\Phi}{dz^2} + \left[\frac{N^2(z)}{(U-c)^2} - \frac{d^2U/dz^2}{U-c} - k^2\right]\Phi = 0, \Phi(0) = \Phi(-H) = 0. \tag{3}$$

Here Φ is the modal structure function, k is the wavenumber (also called the nonhydrostatic term), and H is the local depth, which must be considered constant (see e.g. Miles, 1961; Smyth et al., 2011).

We next present Froude numbers estimated near the sill at different moments in time at the positions where the signatures of the ISWs were identified in the model. Note that the local depth H was chosen accordingly when solving the BVP (3). Starting after the maximum westwards tidal flow, when the Froude numbers are higher in magnitude since tide and SEC add constructively, Fig. 5a shows that the flow is never nearly critical (nor supercritical) for mode-1 IWs corresponding to the scales of the disturbances identified in the model (i.e., $|Fr_1| < 1$). This means that they are not arrested by the tidal (+SEC) flow over the sill, being capable to propagate away from the eastern flank of the sill as free waves soon after their generation. The feature that gives origin to the mode-1 ISWs (see fragment BA in Fig. 6) can actually be interpreted as a multimodal structure somewhat similar to the structures reported in e.g. Stashchuk and Vlasenko (2007). In fact, Fig. 6 reveals the formation of two systems of waves above the shallowest part of the sill, i.e. fragment BA, and above the westward slopes, fragment L. Subsequently, fragment BA appears to disintegrate into fragment A (the wavefront that leads to the formation of mode-1 ISWs) and fragment B (see Fig. 2), which itself appears to be a multimodal structure formed primarily of a bulged mode-2 wave given the elevations and depressions of isopycnals that can be identified in Fig. 6. Note that these bulged isopycnals (i.e. groups of lines of equal wave phase corresponding to simultaneous elevations and depressions) are slightly inclined upstream, a feature found to be inherent to a superposition of several baroclinic modes propagating upstream (see e.g. Baines, 1995). The Froude number with respect to mode-2 IWs calculated from following the bulge-like mode-2 structure is shown in Fig. 5 (green curves). The Froude number in the first case (corresponding to flow including the SEC) is estimated to be $|Fr_2| \geq 1$ during part of the tidal cycle, thus becoming actually supercritical. This means that the mode-2 ISW-like wave is arrested over the sill, being able to grow in amplitude absorbing energy from the mean flow and becoming a large-amplitude wave. The subcritical condition for the first-mode and supercritical for the second-mode waves result in the splitting of the compact multimodal wave fragment BA into the two broad wave systems, A and B, since the mode-1 wave can freely propagate from the place of generation (i.e. near Xe) while B is still arrested for some time there.

3.1.2. *Mode-2 lee waves over the western part of the ridge*

Over the 400 m isobath at the western crest of the sill (i.e. $X \approx 710$ km in the model coordinate system), a significant depression of the deepest isopycnal can also be seen in Fig. 6, going downwards for some 100 m. Coincidently in space with these isopycnal depressions there is a clear raise of the uppermost isopycnal (1023.1) in Fig. 6. All those (downward and upward) displacements tend to return to their equilibrium levels roughly 5 km downstream (i.e. to the west). This lee wave can be identified also in the velocity field as a bulge-like feature of eastward velocities centred at 150 m depth located between the 1023.1 and 1026.1 isopycnals, accompanied by westward velocities immediately outside of that layer (Fig. 6). This feature is consistent with a mode-2 signature marked by a widening of the pycnocline, which is indicated in the top of Fig. 6 as fragment L. The progression of the mode-2 lee wave identified to form in Fig. 6 is seen to evolve upstream in Fig. 2b–f. This feature can be followed for at least 4 h in the model fields particularly in the density contours (Fig. 2a–e, indicated with vertical dashed lines), moving in the upstream direction (i.e. eastwards) for about 10 km in that period. An average propagation speed for this mode-2 wave after being released is 0.7 m/s.

SAR evidence of these sill-crossing wave features along the 120°T direction is provided by satellite synergy observations (TerraSAR-X and ENVISAT-ASAR acquired on the same day, with a 4 h interval). Fig. 7a provides an example of these mode-2 lee waves (labelled L and L*, respectively), in which it can be seen that ISW-like waves show up as dark bands preceding bright bands along their direction of propagation (refer to the explanation of mode-2 ISW SAR signatures in e.g. Mercier et al., 2012 and Jackson et al., 2012). These are indeed mode-2 waves as it is further illustrated in Fig. 7b, which shows the radar backscatter profile (black curve) across the lee wave crest in the TerraSAR-X image (along the model transect shown in red in Fig. 7a, with distance increasing from the west to the east). For comparison with the SAR, a model transect of $-\partial u/\partial x$ (see Eq. (1)) is also displayed in Fig. 7b (red curve). An overall good agreement between the morphologies of these two signatures (i.e. SAR and model) is visible from Fig. 7b, with only a slight mismatch (of $\Delta x \approx 3$ km) between the x-coordinates of those two curves. These mode-2 waves, initially located over the western side of the sill (as shown by the overlaid 1000 m isobath in Fig. 7a, letter L), moved to the east-southeast by approximately 9.3 km in 4 h (letter L* in Fig. 7a), the period between the two satellite acquisitions shown in Fig. 7a. This gives a SAR based averaged phase speed of 0.65 m/s, which compares favourably with the MITgcm model phase speed of 0.7 m/s for this same feature (see above). Note that the SAR signature labelled L* in Fig. 7a (from the ENVISAT satellite acquired 4 h later than the previous TerraSAR-X image) reveals signs of dissipation, being composed of only one ISW-like wave.

It is important to note that the flow over the shallowest part of the sill, i.e. between 710 and 730 km in the model coordinate system, is nearly critical with respect to mode-2 IWs for approximately ± 2 h from maximum westward flow (see inset panel in Fig. 6 with calculated Fr_2 numbers). In fact, the flow is spatially coherent with $|Fr_2| \approx 1$ over the sill's stretch with depths less than 400 m, never reaching however excessively high $|Fr_2|$ values. We further note the appearance of two distinct mode-2 wave structures over this stretch of the sill 2 h after the maximum westward flow (i.e., when the tidal flow is decelerating). Thus, model and SAR data support the idea that two distinct mode-2 wave structures are generated at the westward and eastward sides of the sill (fragments L and B in Figs. 6 and 7a), being both arrested on each side of the sill by the slightly supercritical flow and subsequently released from the place of their generation. We stress that these mode-2 waves do not appear to merge together at any time, i.e. fragment B is not carried away from the place of its generation to the leeward (i.e. westward) side of the sill. At the same time, the disturbance corresponding to the fast mode-1 wave, labelled A in Fig. 2b–f, propagates away from the place of its generation because of the subcritical conditions for mode-1 IWs everywhere over the sill. Its distance from fragment B progressively increases during wave evolution, because of their different phase speeds, i.e. ISW train A, being a mode-1 structure, is faster than ISW train B, which lags behind as confirmed in the SAR (see Fig. 7a letters A* and B*).

3.2. Generation of internal waves in the far field: long-lived mode-2 internal wave features far away from the sill

Some SAR images showed clear signatures of large ISW trains that appeared typically 80 km upstream of the sill (i.e. to the east of Xe) in between the primary ISW mode-1 trains reported earlier, but which could not belong to the same family of those. An example of such features is now presented in Fig. 8a, which corresponds to an ENVISAT-ASAR image (WS mode) dated 28 March 2009 and acquired at 18:17 UTC. In this image, as in many others of its kind, two primary ISW trains consisting of mode-1 ISWs are separated by typically 100–120 km along their propagation direction depending on their travelled distance, as it can be seen in the SAR intensity

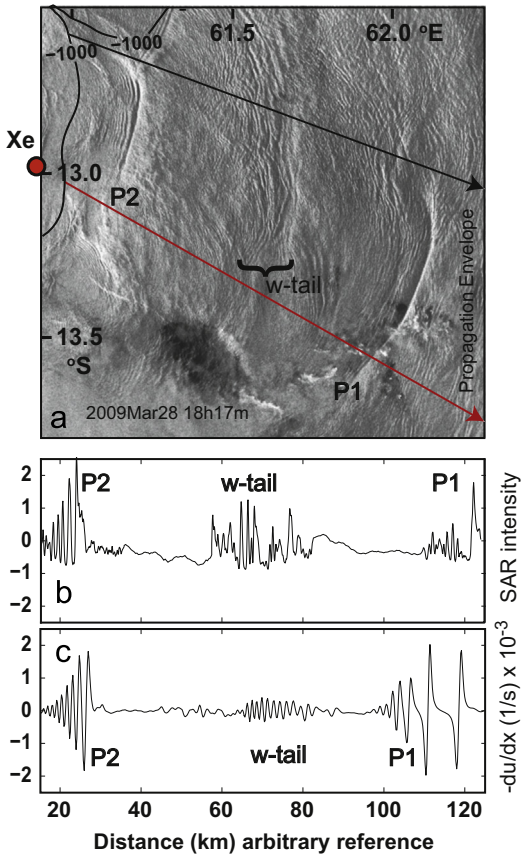

Fig. 8. (a) Subset of an ENVISAT-ASAR image dated March 28 (2009), showing a typical view of the upstream propagating ISW field (Xe and the 1000 m isobath have been added for reference). A propagation envelope containing the sea surface signatures of two mode-1 ISW packets (P1 and P2) and a "wave-tail" is delimited above by a black solid line, and below by the model transect (in red). (b) The backscattered SAR intensity retrieved from any representative transect drawn across the propagating ISWs and defined within the propagation envelope. (c) The same transect, but for the modelled surface velocity gradient along the red line in (a). (For interpretation of the references to color in this figure legend, the reader is referred to the web version of this article.)

transect (relative to the mean NRCS) displayed in Fig. 8b, which is representative of any line crossing the wave trains within the propagation envelope defined by the two solid lines (the top black line and the model transect red line) in Fig. 8a. In that same image (see Fig. 8a and b) one additional wave feature can be noted: a large wave train labelled "w-tail" and whose leading wave is located roughly at 80 km, approximately halfway between the two primary ISW trains (labelled P1 and P2), and whose total length along the propagation direction is at least 20 km. This wave train has backscatter cross section variations comparable to the primary ISWs (in terms of signal amplitude, see Fig. 8b).

The radar signatures of these secondary ISW trains (labelled "w-tail" in Fig. 8b) are characteristic of mode-1 ISWs of depression, and are similar in many aspects to those reported in Guo et al. (2012) and referred by those authors as "*short-scale mode-1 ISWs riding on larger-scale mode-2 internal waves*". This specific description "coined" in Guo et al. (2012) and Vlasenko et al. (2010) originates from the fact that these shorter-scale waves defining the trailing "wave-tails" are in fact propagating on the background of a larger-scale mode-2 IW with the same phase speed. In fact, these short-scale ISWs were found to be confined to the upper 500 m of the water column, i.e. an upper-layer wave duct, where the horizontal velocity structure of their companion mode-2 IWs allows oscillatory solutions of the Taylor–Goldstein eigenvalue problem. Below that layer the solutions to the Taylor–Goldstein

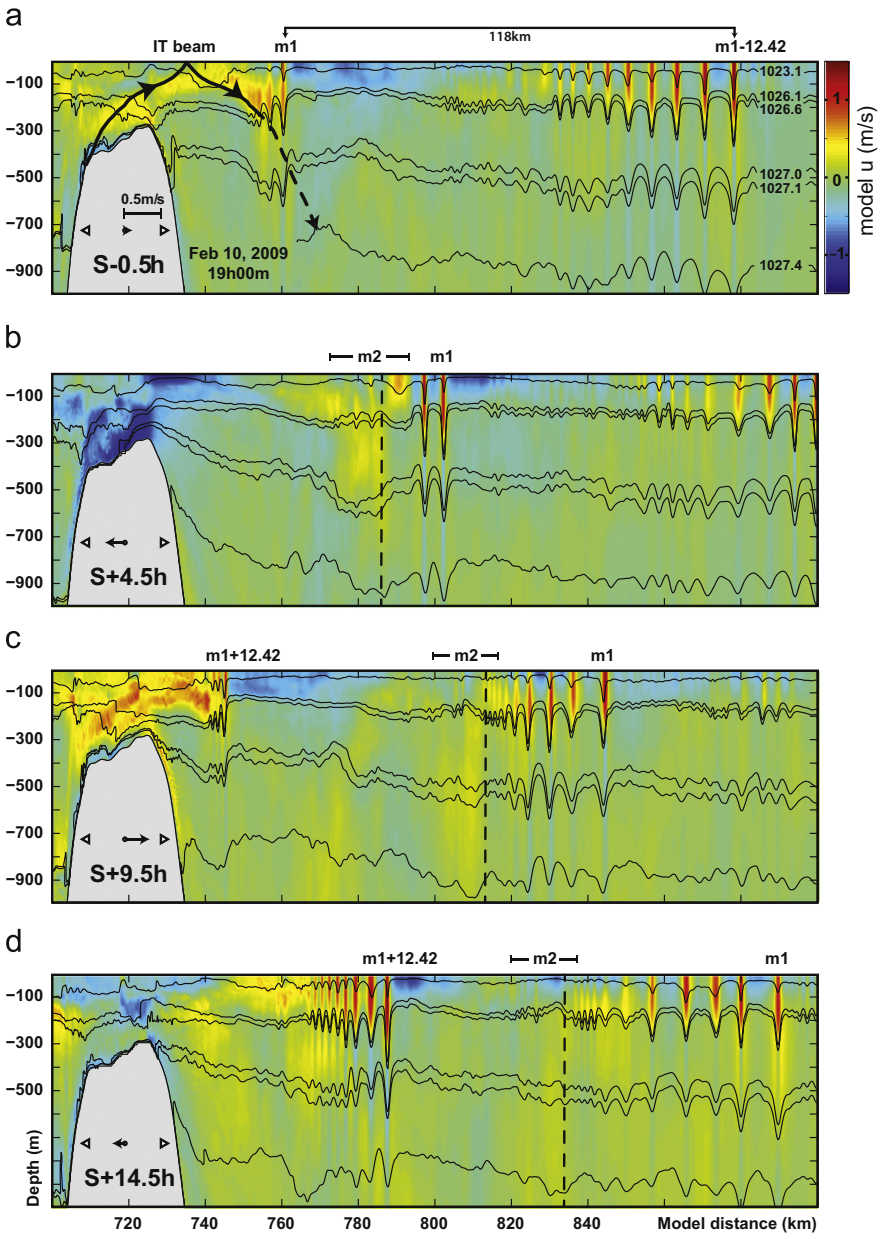

Fig. 9. Same as Fig. 2 for a time sequence of 15 h but extending farther upstream. Reference locations for mode-1 (m1), and mode-2 (m2 and vertical dashed lines) waves are added on top of each panel. Note that top panel also shows the predicted geometry of an internal tidal beam formed on the western slopes of the sill (see black line, with arrows indicating direction of energy propagation). (For interpretation of the references to color in this figure, the reader is referred to the web version of this article.)

eigenvalue problem are evanescent, i.e. decaying exponentially. This argument is based on the Scorer (1949) parameter and often used to study wave ducting in the atmosphere.

We next compute $-\partial u/\partial x$ (see Eq. (1)) for the surface level of the model, which is presented in Fig. 8c. As it can be seen, the model's signal morphology is quite similar to the radar transect presented in Fig. 8b, the main difference being the smaller relative amplitude of the "w-tail" in Fig. 8c. Before proceeding, we want to stress however the remarkably good qualitative match between model and SAR data. This fact provides significant confidence in that the present model is reliable and reproduces the main physical features of the nonlinear IW field on the upstream side of the Mascarene Plateau. In what follows we will then describe the main dynamic features seen in the 2D vertical sections of the model.

Vertical sections with model data of the top 1000 m of the water column for a distance of about 200 km upstream of the sill are presented sequentially in Fig. 9, which span a total period of 15 h. During that period the formation and evolution of the primary mode-1 ISW trains are easily identified both in the horizontal velocity and isopycnal fields. Isopycnal depressions in the form of ISWs are characterized by amplitudes exceeding 200 m. We now turn our attention to smaller wave features that are also apparent in the model. A dashed vertical line is marked in Fig. 9 (panels b–d) and labelled m2. The horizontal velocity pattern to each side of that vertical line together with the isopycnal displacements in the top 1000 m are in fact revealing of a mode-2 IW. Note that the horizontal velocity alternates twice around zero in the vertical, and once in the horizontal precisely across the vertical dashed lines. Such velocity patterns, together with convex and concave shapes of the corresponding isopycnals, particularly visible in part b of Fig. 9 around the mid water depth, can unambiguously be interpreted as mode-2 propagating IWs. In addition, the speed derived from the advance with time of these features (estimated from the dashed vertical lines in panels b–d) is consistent with those of mode-2 nonhydrostatic

short linear IWs based on the solution of the Taylor–Goldstein eigenvalue problem, as will be shown below.

When we extrapolate backwards (in time) the propagation path of these mode-2 IWs we should expect to find a generation location and tidal phase for their origin. This coincides in Fig. 9a with an internal tide ray trajectory which is overlaid on the model section, being computed from its slope s to the horizontal, given by:

$$s = \pm \left(\frac{\omega^2 - f^2}{N^2 - \omega^2} \right)^{\frac{1}{2}} \quad (4)$$

where N is the local Brunt–Väisälä frequency, ω is the semidiurnal frequency, and f the Coriolis parameter. The ray origin corresponds to critical slopes on the western flank of the sill, i.e. where the seafloor slope matches the local value of s. This is where we expect generation of internal tidal waves as the seafloor slopes are subcritical upstream and supercritical downstream of that position. The coherent velocity structure (yellow coloured) seen in Fig. 9a, which has the same path as the IT ray trajectory, is similar to the internal tide simulations reported in Gayen and Sarkar (2010), see e.g. their Figure 1a and Kanarska et al. (2007, see their Figure 13c). In this case, the beam reflects from the sea surface and then propagates downwards and eastwards (see also movie in Supplementary material). Such feature extends in the upstream direction at least as far as $X=750$ km in the model coordinate system, and appears to impinge from above into the pycnocline layer, i.e. more precisely in the proximity of the 2nd and 3rd uppermost isopycnals in Fig. 9a, in a location close to (but still to the west of) the position of the mode-1 ISW train that has already developed from the density front illustrated in Fig. 2a. A plausible explanation for the generation of a mode-2 IW at this location is presented in Section 4.

Supplementary material related to this article can be found online at http://dx.doi.org/10.1016/j.dsr.2015.01.002.

Next we will further examine the existence of mode-2 IWs that propagate eastward, assessing their longevity and investigating their generation mechanisms. Once more, we assemble a travel–time graph with SAR observations and compare them with the model simulations. Fig. 10 shows model data points (in green) for mode-2 IWs travelling upstream (i.e. eastwards) of the sill as well as the SAR leading signatures (in red) of "wave-tails" similar to those in Fig. 8a. The data points comprise approximately 30 h (i.e. more than 2 complete semi-diurnal tidal cycles) and reach to about 150 km away from the sill. The travel–time graph is assembled in the same manner as it has been done for mode-1 ISWs and described in Section 2. Note the model consistency along a linear fit to the SAR data (red line in Fig. 10). Two additional curves are drawn in this travel–time graph: (1) a propagation trajectory for linear mode-1 IWs propagating through variable bathymetry and against the steady SEC current, with the origin at the sill's crest (Xe ≡ 0) by the time of slack tide (i.e., tide reversal from westward into eastward flow), which is obtained by solving the BVP (3) with an appropriate wavenumber (i.e. nonhydrostatic short-waves corresponding to $\lambda=4$ km which are typical length scales observed in the model); and (2) a similar curve but for mode-2 IWs (solutions based on a wavenumber corresponding to $\lambda=20$ km which are typical of these mode-2 waves), whose slope is thus significantly smaller than for mode-1 waves (see lower dark continuous line in Fig. 10). It is then apparent from Fig. 10 that, the slopes of the model data and the SAR linear fit are similar to the slope of the mode-2 linear IWs, but smaller than the slope of the mode-1 IW theoretical curve. In fact, the slope of the data (1.36 m/s from the model) in Fig. 10 almost matches that of mode-2 nonhydrostatic linear waves, being however slightly above than this (owing to nonlinear effects as discussed earlier). We thus conclude that the wave trains in question, which were referred above as "wave-tails", propagate with a phase speed close to (but slightly superior) the mode-2 linear IWs. We also note some additional SAR data points located in the vicinity of the sill's crest, around 10–15 km from the origin and displayed as smaller blue filled circles in Fig. 10. These correspond to SAR signatures of mode-2 ISW-like waves identified in the satellite images (e.g. Fig. 7a, letters L, L* and B*). However these features seem to belong to a different family of mode-2 IWs, as there is a gap of data in the travel–time graph suggesting that the other group of mode-2 waves, which we denominate here as "long-lived" mode-2 waves, are not directly related with this first group (denominated "short-lived"). Indeed, the travel–time diagram suggests that the appearance of the "long-lived" mode-2 IWs occurs some 45–50 km from Xe (i.e. after the location where the IT beam impacts the pycnocline from above, see larger green circle for location in Fig. 10), 8 h after slack tide (i.e. reversal from westward into eastward tidal flow, see also green dashed lines in Fig. 10).

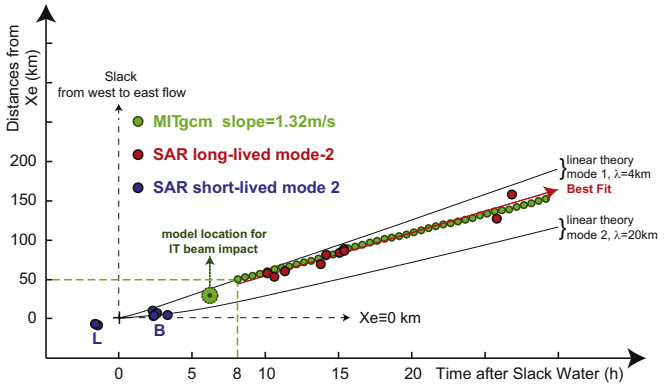

Fig. 10. Travel–time plot for 10 SAR observations (red circles) of internal "wave-tails" (leading wave) and corresponding observations taken from the MITgcm (every half-hour, green circles). A linear fit to the SAR observations (red solid line) is shown together with linear predicted trajectories, assuming generation at Xe either for mode-1 or mode-2 IWs (black lines). Note the additional reference (large green filled circle) for the location of beam impact (see also Fig. 9). An additional set of data points close to Xe (in blue) is shown, and refers to the SAR observations (see text for more details). (For interpretation of the references to color in this figure legend, the reader is referred to the web version of this article.)

The data thus far then seem to support the idea of the existence of three different types of mode-2 IWs: (1) mode-2 internal lee waves that are generated over the western side of the sill, which were described above and labelled L and L* in Fig. 7a and are arrested during the maximum westward tidal flow, (2) short-lived mode-2 IWs generated over the eastern side of the sill during near-critical flow for mode-2 IWs, whose SAR signatures can be identified for at least 5 h and propagate upstream of the sill (those labelled B* in Fig. 7a), and (3) long-lived waves away from the sill that last for at least 22 h. The generation mechanisms of these different types of mode-2 IWs will be further discussed in Section 4.

3.3. *Effects of the steady current*

In the previous Sections all results concerned the superposition of a steady barotropic SEC with tidal currents, as this is the natural scenario encountered in the study region. Next, we briefly discuss what would be the effects of relaxing the simulated SEC to naught. The comments below thus refer to the first experiment (i) introduced in Section 2, when only tidal currents were set into the model (i.e. symmetric currents corresponding to the period of the numerical experiments). Fig. 5 portraits the criticality of the flow for mode-1 and mode-2 IWs. The flow reaches critical conditions only for mode-2 IWs when the SEC is introduced (see Fig. 5a). Without the presence of a steady SEC $|Fr_2| < 1$, as it is shown in Fig. 5b. This confirms what is seen in the model simulations, i.e. that mode-2 lee waves (marked L in Fig. 11a) are not trapped over the sill, thus not being blocked in the place of its generation but propagating upstream soon after their

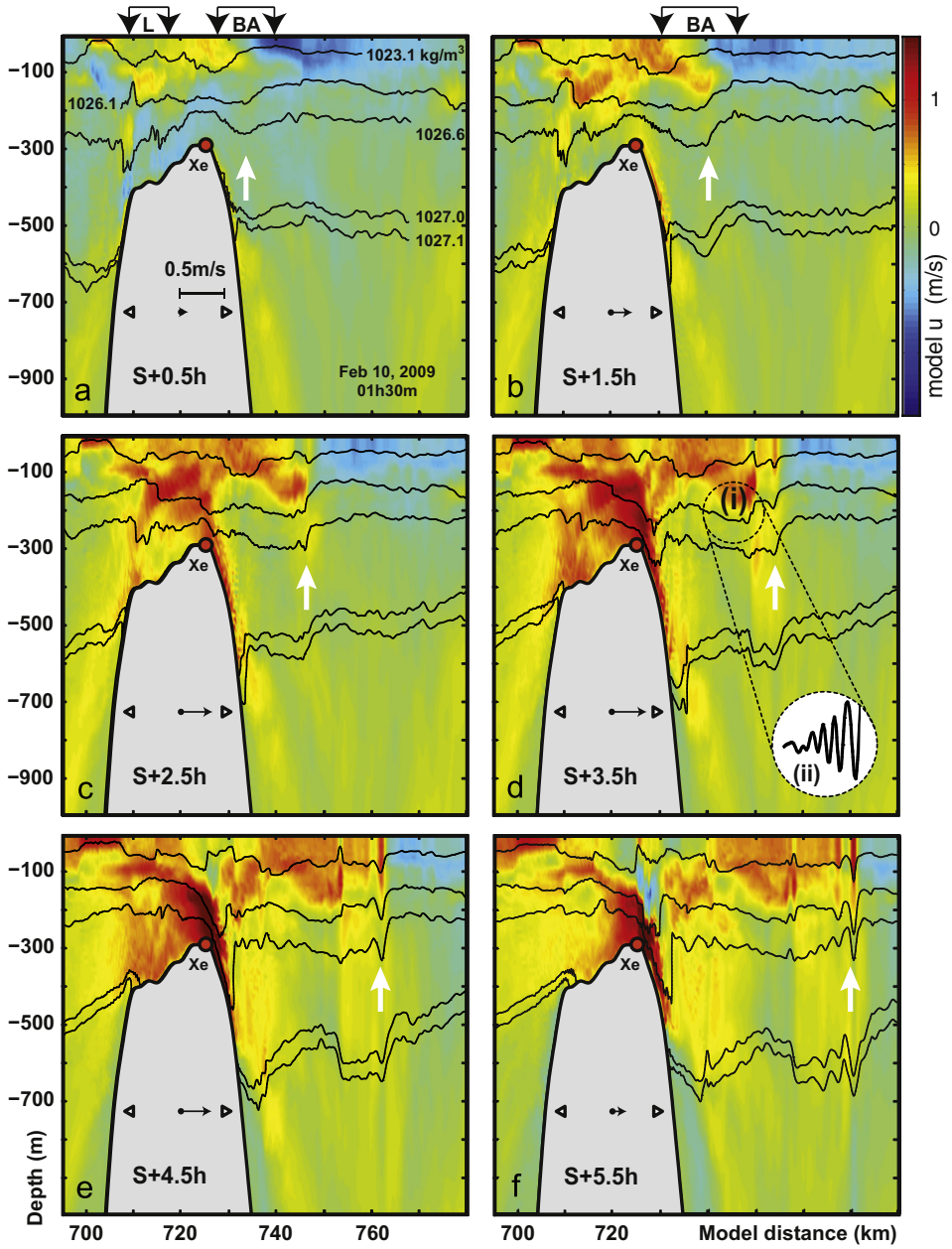

Fig. 11. As for Fig. 2 but for experiment (i). Reference locations tracking the evolution of a lee wave (L), a mode-2 bulge (B) and mode-1 internal wave (A) are shown on top of panels a, b (see text for details). A white arrow is also used to follow a density front disintegrating into a packet of mode-1 ISWs. Part d shows an inset of an ISW train as in Fig. 2f (i.e. for experiment (ii), at the same phase of the tide), for direct comparison with wave evolution in experiment (i).

genesis. Based on numerical experiment (i), they have less time to grow in amplitude by absorbing energy from the background flow. The next distinction is the multimodal baroclinic structure excited upstream that originates both mode-1 and mode-2 ISW-like waves (fragment BA in Figs. 6 and 11a, b), which takes longer to disintegrate into a packet of mode-1 ISWs (see white vertical arrows in Fig. 11). Note that all frames in Fig. 11 are two hours later than frames in Fig. 2, i.e. generally similar features appear in experiment (i) but with a two hour delay compared to experiment (ii). The reason for this is the weaker current (i.e. tides without SEC) which produces only a slightly sloping leading front compared to the steeper front in the case of the tidal flow with the SEC, and thus a longer time is required for its non-linear disintegration. Another difference in the case of tide only forcing is that mode-1 ISWs have slightly smaller vertical amplitudes and form farther upstream. This is clearly seen in Fig. 11d, where an inset shows the position of the mode-1 ISWs for both experiments (i.e., i and ii) at the same tidal phase (slack + 3.5 h). It can be seen that in experiment (ii) ISWs are more developed at this tidal phase. As to the long-lived mode-2 IWs observed in experiment (i), in general they exhibit smaller vertical displacements and are somewhat harder to identify (not shown in Fig. 11), as compared to the basic run case (i.e. experiment-ii including SEC and tides).

4. Discussions

4.1. Generation mechanism of mode-1 and mode-2 ISWs: upstream multimodal structure

New evidence presented in this paper is in contrast with the traditional view of the lee wave generation mechanism, since the first mode-1 waveforms are identified well upstream from the

location of the lee wave forming downstream, and seem to result from an independent process which precedes the relaxation and advance of the lee wave mode-2 structure. We next re-examine the generation mechanism of the primary (i.e. largest) mode-1 ISWs that propagate upstream from the sill (i.e. eastward) described in Section 3.1.1 and observed in da Silva et al. (2011). These were also denominated type-II ISWs in New et al. (2013).

Our numerical experiments suggest that the mode-1 ISWs propagating upstream in the eastward direction are generated by a physical process that includes three distinct phases: (1) the formation and subsequent evolution of an initial multimodal baroclinic structure maintained over the crest of the sill (near the summit, i.e. Xe) during the westward flow of the tide, which evolves into a large density front on the eastern side of the sill near westward-eastward tide transition (this sequence is captured in parts a–c of Fig. 2); (2) nonlinear steepening of the density front into a deep density-waveform of depression (parts d–e in Fig. 2); and (3) evolution of the waveform of depression into a mode-1 ISW train owing to the effects of nonlinearity and dispersion (part f in Fig. 2). This process is not connected with the mode-2 lee wave that is formed further downstream as previously proposed in da Silva et al. (2011) and New et al. (2013). In fact, the mode-1 ISWs travelling east can be interpreted as formed by an "internal tide release" mechanism similar to that described in Buijsman et al. (2010) for ISWs travelling upstream (i.e. to the west) of the Luzon Strait in the SCS. As in the SCS, the flow over the Mascarene ridge is always subcritical ($|Fr_1| < 1$) with respect to mode-1 IWs of the observed spatial scales (see Fig. 5), setting up a long elevation wave to the east of the ridge as a result of blocking (see Baines, 1987). This is a mode-1 long wave that is launched upstream (see grey lines in Fig. 3), gently raising isopycnals in the upper layer (i.e. near the base of the mixed layer), leading to a shoaling of the pycnocline that extends for 10's of km from the sill's crest in the upstream direction. As time progresses further, the pycnocline (to the east of Xe) initially slopes gently downward, gradually steepens, and forms a mode-1 ISW train. All these stages can also be seen in Fig. 2, near the sill's crest, and are similar to the model results presented in Lai et al. (2010) and Scotti et al. (2007) for ISWs on the western side of Stellwagen Bank in Massachusetts Bay, but not with the experimental results of Maxworthy (1979).

While the process of nonlinear transformation of baroclinic bores into packets of nonlinear mode-1 ISWs has been theoretically understood for some time (Lamb, 1994), the present case is distinctive from the usual one because it comprises the disintegration of a multimodal baroclinic structure due to a critical ($|Fr_2| \approx 1$) condition that occurs over the shallowest part of the sill (i.e. position Xe, see fragment BA in Fig. 6). In fact, all the stretch above 400 m depth over the sill (i.e. between 710 and 730 km) is nearly critical for mode-2 IWs for about 4 h during the tidal cycle (see inset in Fig. 6). This means that upstream propagating mode-2 IWs are blocked near their generation site for a considerable time, being able to grow into large-amplitude waves by extracting energy from the background flow, before they are released upstream. Since the mode-1 baroclinic bore excited upstream, i.e. fragment A in Fig. 2b, is not blocked in the place of its generation because the conditions there are always subcritical for mode-1 IWs, it can detach from mode-2 fragment B and evolve free in the upstream direction. The SAR image shown in Fig. 7a, which is typical for the region, testifies precisely that, showing the result of the multimodal bore evolution after a few hours: model fragments A and B evolved both into two distinct packets of ISW-like waves A* and B*.

4.2. Generation and propagation of long-lived mode-2 internal waves

The overall impression from analysis to the travel–time graph presented in Fig. 10, which was introduced in Section 3.2, is that

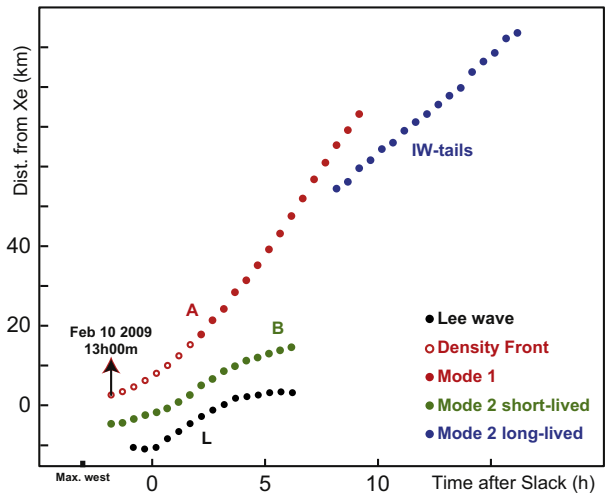

Fig. 12. Travel–time graph comparing the evolution of IWs in the near-field (i.e. the density front disintegration into mode-1 ISWs and short-lived mode-2 features) with the long-lived mode-2 ISW-like waves (i.e. associated IW-tails) identified in the far-field (see labels). All data points in the model are referenced to Xe and Slack Water, and are presented every 30 min after maximum westward flow. Additional labels referring to wave features identified in Figs. 2 and 7 (marked L, A and B) are also shown for reference. (For interpretation of the references to color in this figure legend, the reader is referred to the web version of this article.)

there are at least two different families of mode-2 ISW-like waves: (1) those which are generated over the sill and propagate upstream in its vicinity (i.e. blue filled circles in Fig. 10); and (2) mode-2 IWs that seem to be generated away from the sill and propagate for longer distances and periods of time (red and green filled circles in Fig. 10). It is important to note that the latter wave features identified in the model are considerably larger than the mode-2 IWs that are generated over the sill (i.e. wavelengths typically exceeding 20 km as compared to 5 km). To gain further insight about the origin of these apparently two distinct families of mode-2 ISW-like waves, we assemble a travel–time graph based on following all leading wave features in the model time series in the upstream direction. This is shown in Fig. 12, where the multimodal bore (fragment BA in Fig. 2a) is tracked upstream with red and green circles, clearly diverging into two different wave packets of mode-1 and mode-2 ISW-like waves, respectively (letters A and B in Fig. 2). Note that the red circles are initially opened in Fig. 12, meaning that we distinguish the evolutionary stages of the wavefront structure that disintegrates into the series of nonlinear mode-1 ISWs in about 3 h. More importantly, note that the mode-2 ISW-like features tracked in blue circles in the far field are not connected to the mode-2 ISW-like waves that emerge from the splitting of the multimodal bore described above (i.e. B fragments in Figs. 2 and 6; green circles in Fig. 12). This striking revelation, together with the fact that, in the near field the mode-2 IWs can be followed for only about 8 h, compared to over 20 h in the far field (see also Fig. 10), calls for further attention and poses a question: how were these large mode-2 ISW-like features, with horizontal scales of approximately 20 km, generated?

Although the number of observations of mode-2 ISW-like waves in the ocean has been increasing (see e.g. Yang et al., 2009; Ramp et al., 2012) the generation processes of these waves are still being investigated. While some mode-2 ISW-like wave trains may be ephemeral events, being essentially short-lived nonlinear features (e.g. Shroyer et al., 2010; Akylas and Grimshaw, 1992; Farmer and Smith 1980), the existence of long-lived mode-2 IWs were recently predicted in numerical simulations (Vlasenko et al., 2010) and observed with SAR (Guo et al., 2012).

In Fig. 9a an IT beam can be clearly seen, together with its reflection from the sea surface and subsequent propagation

downwards and eastwards. This beam structure then impinges from above into the pycnocline some 50 km upstream of position Xe, approximately at $X=780$ km in the model coordinate system (see transition from Fig. 9a,b). Since upward IT beams emanating from the upper critical slopes of the sill in question have also been predicted in the model results of Morozov and Vlasenko (1996) and Morozov et al. (2009), in what follows we seek for a plausible explanation for the generation of mode-2 ISW-like waves somewhere between $X=750$ and $X=780$ km related with the IT beam interaction with the pycnocline.

Grisouard et al. (2011) considered a Bragg-like resonance condition based on simple geometric arguments to explain the generation of mode-2 ISW-like waves in the pycnocline due to interaction of an IW beam. Denominating this condition by the "near-field" approach, i.e. a method to explain which IW vertical mode would be selected to form along the pycnocline upon beam impact, they focused on the initial phase of wave generation, assuming the dynamics may be linear. Note that, the beam is refracted as it penetrates into the pycnocline, since its frequency and horizontal wavelength remain unchanged (assuming changes in stratification along the z-axis only), whereas the local buoyancy frequency increases towards the pycnocline. Grisouard et al. (2011) showed that, for the vertical structure of a refracted wave in the pycnocline to be similar to that of a mode-2 IW, the horizontal wavelength of the wave beam λ_x must be twice as large as the (integrated) path of an IW characteristic between the boundaries of the pycnocline (i.e. between an appropriate choice of the upper and lower layer of the pycnocline, but see their Fig. 8a). In the study region, the wave beam should then have a dominant horizontal wavelength of $\lambda_x=24$ km for the Bragg condition of a mode-2 pycnocline wave to hold. Thus, we next attempt to verify the horizontal wavelength of the beam in our model results.

Fig. 13a shows a snapshot of the modelled horizontal velocities for 10 February 2009 at 20:00 UTC. It corresponds to approximately one hour before slack tide (eastward to westward transition), when the flow is decelerating, after reaching maximum eastward flow. This corresponds to a period when IWs of several modes are free to propagate eastward and thus consistent with the picture of formation of an IW beam. The beam structure can be clearly seen over the ridge and leaning upstream to the east, which also features a surface reflection at approximately $X=745$ km (see Fig. 13a). This is particularly visible if we follow the pattern corresponding to positive (eastwards) horizontal velocities (in yellow and red colours) emanating from the upper westward slope of the sill (beginning approximately at $X=710$ km and 400 m deep in Fig. 13a). The beam keeps its coherence from at least 1 h before slack and can be seen in the horizontal velocity field well after slack. This is visible in Fig. 13b where we plot the time evolution of the horizontal velocity field along a horizontal section that intersects the beam at $z=-105$ m between $X=710$ km and $X=740$ km (i.e. a horizontal section across the beam's upward pathway, see dotted vertical lines in Fig. 13a). This horizontal section is roughly 30 km wide and is chosen to span for approximately one wavelength of the IT beam. Furthermore, Fig. 13b reveals a propagating sinusoidal structure of the horizontal velocity across the beam width, which is consistent with the horizontal scale of a typical IT beam in the ocean (e.g. Gerkema, 2001; Mercier et al., 2012). More important is the fact that the beam horizontal wavelength (around 25–30 km) is close to the estimated wavelength of a beam for optimum excitation of mode-2 pycnocline waves (i.e. 24 km, as seen above).

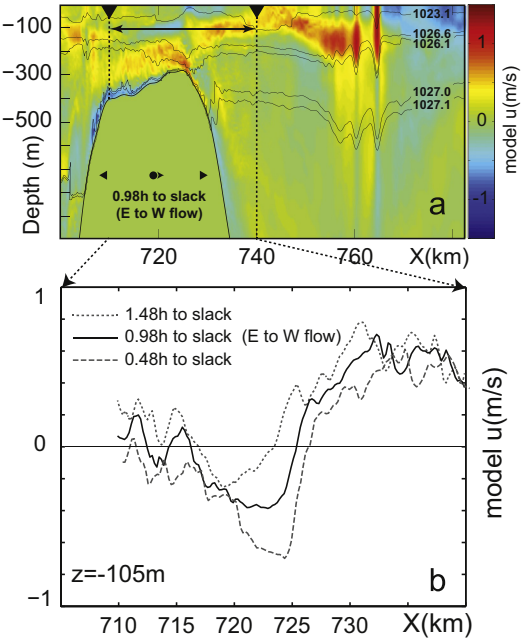

Fig. 13. (a) Zoomed horizontal velocities and selected isopycnals (for February 10, 2009, approximately at slack minus 1 h) highlighting the coherence of a tidal beam structure (in yellow and red colours) that forms on the west critical slopes of the sill and propagates upwards until it reflects from the surface around $X=745$ km. (b) Time sequence of modelled horizontal velocities taken between the vertical dashed lines in (a) at a depth of 105 m. Note the coherence of the near sinusoidal profiles between 1.5 and 0.5 h prior to slack tide, indicating the horizontal wavelength dimensions of the beam. (For interpretation of the references to color in this figure legend, the reader is referred to the web version of this article.)

To further examine what vertical mode will be selected to evolve from the beam impact with the pycnocline, another method is tested, based on the works of Grisouard and Staquet (2010) and Grisouard et al. (2011). This consists of evaluating which mode will be effectively trapped in the pycnocline by computing the phase speeds of possible trapped modes, and comparing these with the forcing beam horizontal phase speed. Since ISWs evolve from interfacial trapped waves in the pycnocline, i.e. whose frequencies are comprised between some lower layer threshold N_0 and the maximum value of $N(z)$, Grisouard and Staquet (2010) computed the phase speeds of the lowest modes as a function of increasing frequency (i.e. for waves increasingly confined close to the pycnocline) searching for the wave mode whose phase speed matched the IT beam horizontal phase speed. This was denominated the "far-field condition" in Grisouard et al. (2011), who compute the phase speeds of the trapped modes via a normal mode approach, using a real stratification profile $N(z)$. Here we follow their method and find solutions of the Taylor–Goldstein eigenvalue problem (3), along with boundary conditions consisting of a flat bottom and a rigid lid, for increasing frequencies starting from the M_2 (semi-diurnal tidal) frequency. The horizontal phase speed of the IT beam, whose frequency matches the semi-diurnal tide, is estimated by measuring the dominant horizontal wavelength of the beam from the model (see Fig. 13), which is found between 25 and 30 km. The estimated phase speeds are thus within the interval 0.55–0.67 m/s. Assuming the same background stratification of the eastern Mascarene Plateau (shown in Fig. 1d), we compute the phase speeds of the two lowest vertical modes, which are displayed in Fig. 14. For frequencies considerably higher than the Brunt–Väisälä frequency outside the seasonal pycnocline (i.e. corresponding to the right end of the frequency axis in Fig. 14), the modal phase speeds weakly vary (i.e., they can be considered constant for each vertical mode), thus corresponding to the "trapped phase speed". In this "trapped" regime (coloured in grey in Fig. 14), IWs of such frequencies could not propagate outside the pycnocline, thus being confined to propagate along the pycnocline. As it can be seen from Fig. 14, the modal phase speed that best matches the horizontal phase speed of the IT beam is that corresponding to a mode-2 IW at frequencies 20–25 times the semi-diurnal frequency. As already proposed by Grisouard et al. (2011), the emergence of a particular vertical pycnocline mode is dictated by the proximity of the horizontal

phase speed of the IT beam to the phase speed of this mode. However, the mode-2 nonlinear structure which is observed in the model, i.e. indicated with a dashed vertical line in Fig. 9, appears with a frequency of only about 5 times the (M_2) semi-diurnal frequency. This means that such mode-2 wave would be free to propagate along a rather broad wave duct, i.e. down to O (1000 m), which is in fact observed in the model (see Fig. 9). Clearly, further investigation is required to understand these new details of the local generation mechanism, and how it is operating in the ocean. For instance, it is also important to recall that Grisouard and Staquet (2010) discuss the importance of horizontal shear flow (e.g. associated with the larger scale IT) in the local generation process and in the ducting stages of these waves. Moreover, nonlinear simulations of the refraction of an IW beam with a finite thickness pycnocline have recently revealed the generation of several IW harmonics confined to the pycnocline (Wunsch et al., 2014; Diamessis et al., 2014), which may also be associated to the local generation of ISW-like waves (see further details about the local generation of ISWs in Dossmann et al., 2013; Mercier et al., 2012; Grisouard et al., 2011; Grisouard and Staquet 2010; Akylas et al., 2007; Gerkema 2001; New and Pingree 1990, 1992).

Here we suggest that the generation of mode-2 IWs at approximately 50 km upstream from the summit of the sill (position Xe), which propagate along a broad horizontal wave duct stretching from near the surface down to at least O (1000) m, is a result of the impact of the IW beam with the pycnocline. Subsequently, shorter-scale waves (or "wave-tails") develop on the background of the larger-scale mode-2 IWs, propagating with the same phase speed as the mode-2 waves but presenting a mode-1 structure, both in the SAR and the model, as seen in Section 3.2. We note that this is somewhat similar to the mechanism described in Grisouard and Staquet (2010), where the propagation speeds and distance between trains of mode-1 ISWs are controlled by the presence of an interfacial long wave, which is probably the manifestation of a mode-3 IT in the upper layers of the Bay of Biscay (see also e.g. Pingree et al., 1986). Those short-period "wave-tails" have an intrinsic frequency of 20–25 times the semi-diurnal frequency, being confined to the upper layers above 500 m. Furthermore, as

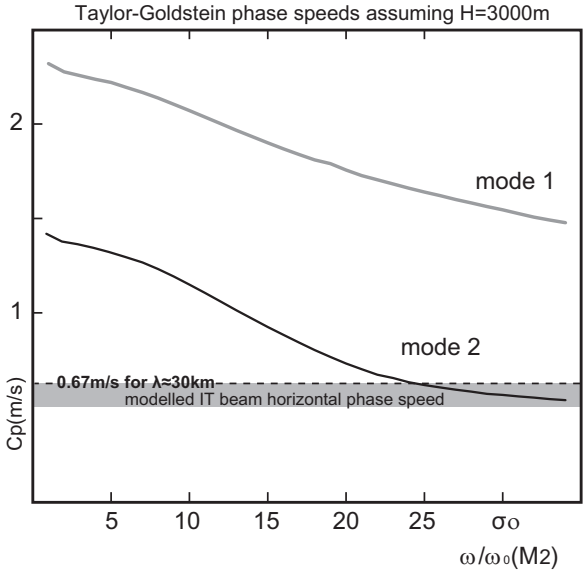

Fig. 14. Comparison of the IT beam horizontal phase speed (set between 0.55 and 0.67 m/s, see shaded area) with the Taylor–Goldstein BVP predicted phase speeds for the first two vertical modes vs. frequency (normalized by the semi-diurnal frequency, ω_o), using a stratification profile typical of the eastern Mascarene Plateau. Grey shaded area indicates the trapped regime. See text for more details.

was done in Vlasenko et al. (2010), an analysis based on the Taylor–Goldstein eigenvalue problem with boundary conditions (3) (not shown) reveals that this "trapping" effect is reinforced by the particular vertical structure of u within the mode-2 ISW-like vertical profile, which favours wave ducting in the upper layers (essentially when considering the nonhydrostatic linear theory, i.e. oscillatory solutions predicted by the BVP). Below this ducting layer the shorter-scale ISWs cannot propagate, since the deeper horizontal velocity associated with the mode-2 IW changes sign, contributing only to an exponential decay in wave energy. This can be seen in Fig. 9 where the presence of "wave-tails" (see e.g. panel d around 840 km) is confined to the upper layers above 500 m. This ducting role given by the mode-2 IWs presumably allows for the longevity of the "wave-tails", which are observed in the SAR hundreds of km away from their expected generation, as suggested by Guo et al. (2012) for observations in the SCS. Note that this kind of wave-resonance occurs when the mode-1 and mode-2 phase speeds are close, a condition that is favoured because of the particular vertical structure within the larger-scale mode-2 ISW-like wave and the short-scale mode-1 ISWs trapped inside their upper layers. Other examples of resonance involving energy transfer between mode-1 and mode-2 ISWs, including nonlinear coupling, are described in e.g. Bogucki et al. (2005) and Gottwald and Grimshaw (1999).

Thus, the existence of short-period mode-1 ISWs (i.e. "wave-tails") coupled with (i.e. moving with the same phase speed) second mode IWs has been predicted by numerical modelling with the MITgcm and is in agreement with ducting solutions of the Taylor–Goldstein eigenvalue problem with boundary conditions (3), and further confirmed in the SAR observations (see Section 3.2). A different set of mode-2 (lee) IWs, that are relatively short-lived compared to these, will be discussed next.

4.3. Mode-2 internal (lee) waves downstream of the sill: generation and propagation across the sill

We have seen in Section 3.1.2 that $|Fr_2| \approx 1$ all over the sill's stretch with depths less than 400 m (see inset in Fig. 6) for approximately 4 h. This means that resonant conditions for mode-2 IWs prevail over the sill for a considerable period of time, favouring their generation and growth by extracting energy from the background flow. A remarkable feature of the IW system over the sill is thus the simultaneous generation of two distinct mode-2 ISW-like waves, as can be seen in Fig. 6 (fragments L and B). Note that the upper part of the sill is large enough (i.e. length $>$ 20 km) to harbour two adjacent mode-2 ISW-like waves. As the (westward) tide slackens and becomes subcritical with respect to mode-2 IWs, the energy stored in the lee wave is released in the form of a mode-2 ISW-like wave that can be seen in the SAR, e.g. Fig. 7a, as waves labelled L and L*. These mode-2 ISW-like waves have a limited lifetime in the model, and we suspect that they last for just over a semidiurnal tidal cycle, as judged from SAR analysis. While some of those mode-2 lee waves are seen upstream (i.e. eastwards) of the sill's summit thus surviving the crossing of the sill, they clearly belong to a different family of waves than the large-amplitude (primary) mode-1 ISWs and the (secondary) mode-2 short-lived IWs (labelled B) that evolve from the multimodal bore discussed in Section 4.1. In fact, the simultaneous generation and evolution of two mode-2 ISW-like waves over the sill (i.e. fragments L and B) is a distinct characteristic of the Mascarene Ridge, e.g. in comparison with the Knight Inlet (Stashchuk and Vlasenko, 2007) and the SCS (Buijsman et al., 2010).

4.4. Overall view of the generation processes upstream of the Mascarene Ridge

Finally, we compare the IW generation regime in the Mascarene Ridge with other relevant locations where IWs have been intensely

investigated, namely the SCS (west of Luzon Strait) and Knight Inlet (British Columbia, Canada). Table 1 shows some non-dimensional parameters that have been widely used to classify IW generation regimes: the densimetric Froude number (Fr), the topographic Froude number (Fr_t), and the tidal excursion length (δ). As we have seen, the densimetric Froude number lies within the slightly supercritical regime for mode-2 IWs (and supercritical for all higher modes) and in the subcritical regime for mode-1 IWs. This is similar to the case of the SCS, while in Knight Inlet the flow is clearly supercritical for mode-2 (and all higher) modes (see Stashchuk and Vlasenko, 2007). The topographic Froude number is O(100), meaning that significant blocking occurs. While partial blocking occurs in all three sites and is ultimately responsible for ISW generation, the measure of blocking given by Fr_t for the Mascarene Ridge is closer to the SCS case than the Knight Inlet. The tidal excursion length translates how much of the topography of the upper sill is ranged by the tidal flow. It is clear from Table 1 that the tidal excursion length is small compared to the width of the sill in the case of the Mascarene Ridge and the SCS, while in the case of Knight Inlet these lengths are comparable. Therefore, the consistency between these parameters for the SCS and the Mascarene Ridge is in agreement with similar generation scenarios, where tidal beams, lee waves, and the internal tide release mechanism can all coexist. Indeed, while mode-1 ISWs and mode-2 ISW-like waves are generated in the vicinity of all three sites, the generation of mode-2 ISW-like waves by tidal beams is a possibility only in the Mascarene Ridge and the Luzon Strait. Furthermore, the generation of mode-1 ISWs upstream of the sill is a common factor between all these three sites, and we recall, that this is further supported since none of these sites is in the regime where $|Fr_1|$ is much greater than 1.

5. Summary and conclusion

The Mascarene ridge in between the Saya de Malha and Nazareth banks belongs to a mixed-tidal-lee wave generation regime, where the internal tide release mechanism, lee wave generation and local generation of ISWs, may all operate together and generate different sets of ISWs. Three types (or "families") of short-period IWs have been identified and studied in detail: (1) Large mode-1 and mode-2 ISW-like waves that form upstream (i.e. eastwards) of the sill during relaxation of the westward tidal flow as a result of the disintegration of a multimodal baroclinic structure; (2) Second mode IWs with trapped short-period mode-1 ISWs that form after the scattering of an IT beam with the pycnocline; (3) Large mode-2 lee waves that form downstream of the sill and propagate upstream after the tidal flow has relaxed to subcritical conditions with respect to mode-2 waves.

We were able to determine the precise location and tidal phase corresponding to the generation of specific sets of ISWs, with mode-1 and mode-2 vertical structures. These were shown to accurately match SAR observations of the region during spring tides, when the nonlinear IW activity is more active. Thus, the model can now be applied to predict wave arrival times and IW parameters, such as amplitudes and phase speeds, for distances up to at least 200 km upstream of the sill, i.e. in the opposite direction of the SEC that flows westwards.

One of the main goals of the paper was to clarify the generation of the largest, here denominated primary, mode-1 ISWs occurring upstream of the sill, which can be attributed to the internal tide release mechanism. This mechanism, which can also be interpreted as a form of "upstream influence", results from the uplifting of the isopycnals higher on the east side of the ridge due to the blocked westward flow, which is subcritical with respect to mode-1 IWs. This generates a long first-mode elevation wave that propagates away from the ridge, which subsequently disperses into ISWs forming on its back slope (see Buijsman et al., 2010). This generation mechanism is also in qualitative agreement with the sequence of events described in the pioneer work of Lee and Beardsley (1974), since the flow-induced density perturbation is formed on the same side as the resulting ISWs (see also Cummins et al., 2003 and Lai et al., 2010). However, the process described above is not the same as that reported in Maxworthy (1979), which operates mostly for supercritical flows with respect to mode-1 IWs and involves the survival of a mode-1 lee wave across a bank or sill (see also, Apel et al., 1985; Brandt et al., 1997).

Over the sill of the Mascarene plateau the flow is indeed supercritical but only with respect to second and higher IW modes, being subcritical with respect to mode-1 IWs at all times. In such conditions, large-scale mode-2 lee waves are formed downstream of the sill, in a similar fashion as those reported in Farmer and Smith (1980) during periods of moderate to strong tides and summer stratification in Knight Inlet, British Columbia (but see Stashchuk and Vlasenko, 2007). When the tidal flow relaxes, those lee waves are able to propagate upstream as coherent features that are nicely captured both in the MITgcm model and the SAR surface signatures. We believe that these waves have a similar character and generation mechanism as those recently reported in Ramp et al. (2012) in the SCS.

Finally, the other main goal of this paper was to report, for the first time, the existence of long-lived mode-2 IWs coupled with "wave-tails" composed of mode-1 smaller-scale ISWs, in the study region. These coherent features can propagate for distances in excess of 200 km to the east side of the sill with typical longevities exceeding two semi-diurnal tidal cycles. The mode-2 IW structures are captured in the SAR mainly due to their associated first mode ISWs (in the same fashion as those reported in Guo et al., 2012). The generation mechanism of these long-lived mode-2 IWs is consistent with a hypothesis known as "local generation" of ISWs (Gerkema, 2001), involving the scattering of an IT beam with the near-surface pycnocline. They are thought to result from the impact of IT beams with the pycnocline some 50 km upstream of the origin of the primary mode-1 ISWs (i.e. the summit of the sill). This IT beam develops in the MITgcm model soon after slack tide (i.e. transition from west to eastward flow), when vertical IW modes are free to propagate upstream (i.e. to the east). It originates on the lee (i.e. westward) side of the sill from critical topographic slopes, leaning upwards and eastwards and reflecting from the sea surface, after which the beam is thought to generate mode-2 ISW-like waves through a resonant process. Further research is needed to confirm or dismiss this hypothesis. These admittedly locally generated mode-2 IWs can then propagate along the pycnocline for long distances, producing a velocity field with favourable conditions for sustaining their associated mode-1 "wave-tails", in the same manner as reported in Guo et al., 2012 and Vlasenko et al., 2010. The phase speeds of the mode-1 "wave-tails" and large mode-2 ISW-like waves are close, permitting a resonance coupling of the two wave systems.

Acknowledgements

We thank both reviewers for their helpful comments, which have helped to greatly improve the paper. We would like to thank Prof. Adrian L. New for kindly hosting our visits to the National Oceanography Centre, Southampton, as well as Prof. Nicolas Grisouard for stimulating discussions about the local generation of Internal Solitary Waves. Jorge Magalhaes is grateful for an FCT research grant (SFRH/BPD/84420/2012). Maarten Buijsman was supported by the Office of Naval Research (ONR) under Grant number ONRDC32025354. We would like to thank ESA Project AOPT-2423 for providing SAR images as well as the German Aerospace Centre (DLR) under Project OCE0056. Jose da Silva and Jorge Magalhaes are grateful to the Federal University of Rio Grande (FURG), Brazil, for hosting sabbatical periods during which this paper was concluded.

Appendix A. Energy budget considerations

Barotropic to baroclinic tidal conversion rates (see e.g. Buijsman et al., 2012) evaluated at the sill amount to about 3 W/m^2 (referring to tidally averaged values integrated horizontally between 690 and 750 km in the model coordinate system, see Fig. 1). The slightly asymmetric tide (owing to the SEC) and ridge geometry cause larger eastward than westward pressure fluxes (i.e. approximately 101 and 72 kW/m east and west of the sill, respectively). These eastward fluxes are about twice as large when compared to those from the Luzon Strait in the SCS (see Buijsman et al., 2012; Buijsman et al., 2014). Hence, the stronger fluxes at the Mascarene Ridge cause the internal tides to break into ISW trains much closer to the ridge than in Luzon Strait. At present we do not have in situ measurements to confirm these simulated fluxes for the Mascarene Ridge. However, the authors note that the ISW amplitudes of the simulations (and other characteristic dimensions – see Table 2) agree well with the observations reported in the literature (see e.g. Sabinin et al., 1992; Konyaev et al., 1995; da Silva et al., 2011; New et al., 2013). In the far field, as we move away from the generation source, the pressure fluxes reduce in magnitude whereas the advective fluxes tend to increase, i.e. to about 25% of the pressure flux some 200 km eastwards of the ridge due to the strong nonlinear ISWs. It is also noteworthy that, despite the forcing and resulting fluxes being large, the fraction of conversion lost to dissipation is about 6% (in the vicinity of the sill, i.e. near the generation region), which is at least a factor of two smaller than in 2D simulations of the double ridge in the SCS (see Buijsman et al., 2012). These smaller rates may be attributed to the fact that the Mascarene Ridge features only a single ridge with smoother topography, when compared to the more intricate double ridge system of the Luzon Strait.

References

Akylas, T.R., Grimshaw, R.H.J., 1992. Solitary internal waves with oscillatory tails. J. Fluid Mech. 242, 279–298. http://dx.doi.org/10.1017/S0022112092002374.

Akylas, T.R., Grimshaw, R.H.J., Clark, S.R., Tabaei, A., 2007. Reflecting tidal wave beams and local generation of solitary waves in the ocean thermocline. J. Fluid Mech. 593, 297–313. http://dx.doi.org/10.1017/S0022112007008786.

Alpers, W., 1985. Theory of radar imaging of internal waves. Nature (London) 314, 245–247. http://dx.doi.org/10.1038/413245a0.

Apel, J.R., Holbrook, J.R., Liu, A.K., Tsai, J.J., 1985. The Sulu Sea internal soliton experiment. J. Phys. Oceanogr. 15, 1625–1651 (doi:10.1175/1520-0485(1985)015 < 1625:TSSISE > 2.0.CO;2).

Azevedo, A., da Silva, J.C.B., New, A.L., 2006. On the generation and propagation of internal waves in the southern Bay of Biscay. Deep-Sea Res. I 53, 927941. http://dx.doi.org/10.1016/j.dsr.2006.01.013.

Baines, P.G., 1984. A unified description of two layer flow over topography. J. Fluid Mech. 146, 127–167. http://dx.doi.org/10.1017/S0022112084001798.

Baines, P.G., 1987. Upstream blocking and airflow over mountains. Ann. Rev. Fluid Mech. 19, 75–97. http://dx.doi.org/10.1146/annurev.fl.19.010187.000451.

Baines, P.G., 1995. Topographic Effects in Stratified Flows. Cambridge Monographs on MechanicsCambridge Univ. Press, New York482.

Bogucki, D.J., Redekopp, L.G., Barth, J., 2005. Internal solitary waves in the coastal mixing and optics 1996 experiment: multimodal structure and resuspension. J. Geophys. Res. 110, C02024. http://dx.doi.org/10.1029/2003JC002253.

Brandt, P., Rubino, A., Alpers, W., Backhaus, J.O., 1997. Internal waves in the Strait of Messina studied by a numerical model and synthetic aperture radar images from the ERS 1/2 satellites. J. Phys. Oceanogr. 27, 648–663 (doi:10.1175/1520-0485(1997)027 < 0648:IWITSO > 2.0.CO;2).

Buijsman, M.C., Kanarska, Y., McWilliams, J.C., 2010. On the generation and evolution of nonlinear internal waves in the South China Sea. J. Geophys. Res. 115, C02012. http://dx.doi.org/10.1029/2009JC005275.

Buijsman, M.C., Legg, S., Klymak, J., 2012. Double ridge internal tide interference and its effect on dissipation in Luzon Strait. J. Phys. Oceanogr. 42, 1337–1356.

Buijsman, M.C., Klymak, J.M., Legg, S., Alford, M.H., Farmer, D., MacKinnon, J.A., Nash, J.D., Park, J.H., Pickering, A., Simmons, H., 2014. Three dimensional double ridge internal tide resonance in luzon strait. J. Phys. Oceanogr. 44, 850–869.

Chereskin, T.K., 1983. Generation of internal waves in Massachusetts Bay. J. Geophys. Res. 88, 2649–2661. http://dx.doi.org/10.1029/JC088iC04p02649.

Cummins, P.F., Vagle, S., Armi, L., Farmer, D.M., 2003. Stratified flow over topography: upstream influence and generation of nonlinear internal waves. Proc. R. Soc. Lond. 459A, 1467–1487. http://dx.doi.org/10.1098/rspa.2002.1077.

da Silva, J.C.B., Ermakov, S.A., Robinson, I.S., 2000. Role of surface films in ERS SAR signatures of internal waves on the shelf. 3. Mode transitions. J. Geophys. Res. 105 (C10), 24089–24104. http://dx.doi.org/10.1029/2000JC900053.

da Silva, J.C.B., New, A.L., Azevedo, A., 2007. On the role of SAR for observing "Local Generation" of internal solitary waves off the Iberian Peninsula. Can. J. Remote Sens. 33, 388–403. http://dx.doi.org/10.5589/m07-041.

da Silva, J.C.B., Helfrich, K.R., 2008. Synthetic aperture radar observations of resonantly generated internal solitary waves at Race Point Channel (Cape Cod). J. Geophys.Res. 113, C11016. http://dx.doi.org/10.1029/2008JC005004.

da Silva, J.C.B., New, A.L., Magalhaes, J.M., 2009. Internal solitary waves in the Mozambique Channel: observations and interpretation. J. Geophys. Res. 114, C05001. http://dx.doi.org/10.1029/2008JC005125.

da Silva, J.C.B., New, A.L., Magalhaes, J.M., 2011. On the structure and propagation of internal solitary waves generated at the Mascarene Plateau in the Indian Ocean. Deep-Sea Res. I 58, 229–240. http://dx.doi.org/10.1016/j.dsr.2010.12.003.

Diamessis, P.J., Wunsch, S., Delwiche, I., Richter, M.P., 2014. Nonlinear generation of harmonics through the interaction of an internal wave beam with a model oceanic pycnocline. Dyn. Atmos. Oceans 66, 110–137.

Dossmann, Y., Auclair, F., Paci, A., 2013. Topographically induced internal solitary waves in a pycnocline: secondary generation and selection criteria. Phys. Fluids 25, 086603.

Egbert, G.D., Erofeeva, S.Y., 2002. Efficient inverse modelling of barotropic ocean tides. J. Ocean. Atmos. Technol. 19, 183–204 (doi:10.1175/1520-0426(2002)019 < 0183:EIMOBO > 2.0.CO;2).

Farmer, D.M., Smith, J.D., 1980. Tidal interaction of stratified flow over the sill in Knight Inlet. Deep-Sea Res. 27A, 239–254. http://dx.doi.org/10.1016/0198-0149(80)90015-1.

Farmer, D.M., Armi, L., 1999a. Stratified flow over topography: the role of small scale entrainment and mixing in flow establishment. Proc. R. Soc. Lond. 455A, 3221–3258.

Farmer, D.M., Armi, L., 1999b. The generation and trapping of solitary waves over topography. Science 283, 188–190. http://dx.doi.org/10.1126/science.283.5399.188.

Gayen, B., Sarkar, S., 2010. Turbulence during the generation of internal tide on a critical slope. Phys. Rev. Lett. 104, 218502 (0031-9007/10/104(21)/218502(4).

Garrett, C., Kunze, E., 2007. Internal tide generation in the deep ocean. Annu. Rev. Fluid Mech. 39, 57–87. http://dx.doi.org/10.1146/annurev.fluid.39.050905.110227.

Gerkema, T., 2001. Internal and interfacial tides: beam scattering and local generation of solitary waves. J. Mar. Res. 59, 227–255. http://dx.doi.org/10.1357/002224001762882646.

Gottwald, G., Grimshaw, R., 1999. The formation of coherent structures in the context of blocking. J. Atmos. Sci. 56, 3640–3662.

Grimshaw, R.H.J., Smyth, N., 1986. Resonant flow of a stratified fluid over topography. J. Fluid Mech. 169, 429–464. http://dx.doi.org/10.1017/S002211208600071X.

Grisouard, N., Staquet, C., 2010. Numerical simulations of the local generation of internal solitary waves in the Bay of Biscay. Nonlinear Process. Geophys. 17, 575–584. http://dx.doi.org/10.5194/npg-17-575-2010.

Grisouard, N., Staquet, C., Gerkema, T., 2011. Generation of internal solitary waves in a pycnocline by an internal wave beam: a numerical study. J. Fluid Mech. 676, 491–513http://dx.doi.org/10.1017/jfm.2011.61.

Grue, J., Friis, H.A., Palm, E., Rusås, P.-O., 1997. A method for computing unsteady fully nonlinear interfacial waves. J. Fluid Mech. 351, 223–252. http://dx.doi.org/10.1017/S0022112097007428.

Guo, C., Vlasenko, V., Alpers, W., Stashchuk, N., Chen, X., 2012. Evidence of short internal waves trailing strong internal solitary waves in the northern South China Sea from synthetic aperture radar observations. Remote Sens. Environ. 124, 542–550. http://dx.doi.org/10.1016/j.rse.2012.06.001.

Haury, L.H., Briscoe, M.G., Orr, M.H., 1979. Tidally generated internal wave packets in Massachusetts Bay. Nature 278, 312–317. http://dx.doi.org/10.1038/278312a0.

Jackson, C.R., da Silva, J.C.B., Jeans, G., 2012. The generation of nonlinear internal waves. Oceanography 25 (2), 108–123. http://dx.doi.org/10.5670/oceanog.2012.46.

Kanarska, Y., Shchepetkin, A., McWilliams, J., 2007. Algorithm for non-hydrostatic dynamics in the regional oceanic modelling system. Ocean Model. 18 (3–4), 143–174.

Klymak, J.M., Legg, S., 2010. A simple mixing scheme for models that resolve breaking internal waves. Ocean Model. 33, 224–234. http://dx.doi.org/10.1016/j.ocemod.2010.02.005.

Klymak, J.M., Legg, S.M., Pinkel, R., 2010. High-mode stationary waves in stratified flow over large obstacles. J. Fluid Mech. 644, 321–336. http://dx.doi.org/10.1017/S0022112009992503.

Konyaev, K.V., Sabinin, K.D., Serebryany, A.N., 1995. Large-amplitude internal waves at the Mascarene Ridge in the Indian Ocean. Deep-Sea Res. I 42, 2075–2091. http://dx.doi.org/10.1016/0967-0637(95)00067-4.

Kudryavtsev, V., Akimov, D., Johannessen, J., Chapron, B., 2005. On radar imaging ofcurrent features: 1. Model and comparison with observations. J. Geophys. Res. 110, C07016http://dx.doi.org/10.1029/2004JC002505.

Lai, Z., Chen, C., Cowles, G.W., Beardsley, R.C., 2010. A nonhydrostatic version of FVCOM: 2. Mechanistic study of tidally generated nonlinear internal waves in Massachusetts Bay. J. Geophys. Res. 115, C12049. http://dx.doi.org/10.1029/2010JC006331.

Lamb, K.G., 1994. Numerical experiments of internal wave generation by strong tidal flow across a finite amplitude bank edge. J. Geophys. Res. 99, 843–864. http://dx.doi.org/10.1029/93JC02514.

Lozovatsky, I.D., Morozov, E.G., Fernando, H.J.S., 2003. Spatial decay of energy density of tidal internal waves. J. Geophys. Res. 108 (C6), 3201. http://dx.doi.org/10.1029/2001JC001169.

Lavelle, J.W., Thacker, W.C., 2008. A pretty good sponge: dealing with open boundaries in limited-area ocean models. Ocean Model. 20, 270–292. http://dx.doi.org/10.1016/j.ocemod.2007.10.002.
Lee, C.-Y., Beardsley, R.C., 1974. The generation of long nonlinear internal waves in a weakly stratified shear flow. J. Geophys. Res. 79, 453–462. http://dx.doi.org/10.1029/JC079i003p00453.
Legg, S., Klymak, J., 2008. Internal hydraulic jumps and overturning generated by tidal flow over a tall steep ridge. J. Phys. Oceanogr. 38, 1949–1964. http://dx.doi.org/10.1175/2008JPO3777.1.
Marshall, J., Hill, C., Perelman, L., Adcroft, A., 1997. Hydrostatic, quasi-hydrostatic, and nonhydrostatic ocean modeling. J. Geophys. Res. 102, 5733–5752. http://dx.doi.org/10.1029/96JC02776.
Matsuura, T., Hibiya, T., 1990. An experimental and numerical study of internal wave generation by tide–topography interaction. J. Phys. Oceanogr. 20, 506–521 (doi:10.1175/1520-0485(1990)020 < 0506:AEANSO > 2.0.CO;2).
Maxworthy, T., 1979. A note on internal solitary waves produced by tidal flow over a three-dimensional ridge. J. Geophys. Res. 84 (C1), 338–346. http://dx.doi.org/10.1029/JC084iC01p00338.
Maxworthy, T., 1980. On the formation of nonlinear internal waves from the gravitational collapse of mixed regions in two and three dimensions. J. Fluid Mech. 96, 47–64. http://dx.doi.org/10.1017/S0022112080002017.
Melville, W.K., Helfrich, K.R., 1987. Transcritical two-layer flow over topography. J. Fluid Mech. 178, 31–52. http://dx.doi.org/10.1017/S0022112087001101.
Mendes, R., Vaz, N., Fernández-Nóvoa, D., da Silva, J.C.B., deCastro, M., Gómez-Gesteira, M., Dias, J.M., 2014. Observation of a turbid plume using MODIS imagery: the case of Douro estuary (Portugal). Remote Sens. Environ. 154, 127–138. http://dx.doi.org/10.1016/j.rse.2014.08.003.
Mercier, M.J., Mathur, M., Gostiaux, L., Gerkema, T., Magalhaes, J.M., da Silva, J.C.B., Dauxois, T., 2012. Soliton generation by internal tidal beams impinging on a pycnocline: laboratory experiments. J. Fluid Mech. 704, 37–60. http://dx.doi.org/10.1017/jfm.2012.191.
Miles, J.W., 1961. On the stability of heterogeneous shear flows. J. Fluid Mech. 10 (4), 496–508.
Morozov, E.G., Vlasenko, V.I., 1996. Extreme tidal internal waves near the Mascarene Ridge. J. Mar. Syst. 9, 203–210. http://dx.doi.org/10.1016/S0924-7963(95)00042-9.
Morozov, E.G., Nechvolodov, L.V., Sabinin, K.D., 2009. Beam propagation of tidal internal waves over a submarine slope of the Mascarene Ridge. Oceanology 49 (6), 745–752. http://dx.doi.org/10.1134/S0001437009060010.
Nakamura, T., Awaji, T., Hatayama, T., Akitomo, K., Takizawa, T., Kono, T., Kawasaki, Y., Fukasawa, M., 2000. The generation of large-amplitude unsteady lee waves by subinertial K1 tidal flow: a possible vertical mixing mechanism in the Kuril Straits. J. Phys. Oceanogr. 30, 1601–1621 (doi:10.1175/1520-0485(2000)030 < 1601:TGOLAU > 2.0.CO;2).
New, A.L., Pingree, R.D., 1990. Large-amplitude internal soliton packets in the central Bay of Biscay. Deep-Sea Res. 37, 513–524. http://dx.doi.org/10.1016/0198-0149(90)90022-N.
New, A.L., Pingree, R.D., 1992. Local generation of internal soliton packets in the central Bay of Biscay. Deep-Sea Res. 39, 1521–1534. http://dx.doi.org/10.1016/0198-0149(92)90045-U.
New, A.L., da Silva, J.C.B., 2002. Remote-sensing evidence for the local generation of internal soliton packets in the central Bay of Biscay. Deep-Sea Res. I 49, 915–934. http://dx.doi.org/10.1016/S0967-0637(01)00082-6.
New, A.L., Alderson, S.G., Smeed, D.A., Stansfield, K.L., 2007. On the circulation of water masses across the Mascarene Plateau in the South Indian Ocean. Deep-Sea Res. I 54, 42–74. http://dx.doi.org/10.1016/j.dsr.2006.08.016.
New, A.L., Magalhaes, J.M., da Silva, J.C.B., 2013. Internal solitary waves on the Saya de Malha bank of the Mascarene Plateau: SAR observations and interpretation. Deep-Sea Res. I 79, 50–61. http://dx.doi.org/10.1016/j.dsr.2013.05.008.
Osborn, T.R., 1980. Estimates of the local rate of vertical diffusion from dissipation measurements. J. Phys. Oceanogr. 10, 83–89.
Pingree, R.D., Mardell, J.T., New, A.L., 1986. Propagation of internal tides from the upper slopes of the Bay of Biscay. Nature 321, 154–158.
Ramp, S.R., Yang, Y.J., Reeder, D.B., Bahr, F.L., 2012. Observations of a mode-2 nonlinear internal wave on the northern Heng-Chun Ridge south of Taiwan. J. Geophys. Res. 117, C03043. http://dx.doi.org/10.1029/2011JC007662.
Sabinin, K.D., Nazarov, A.A., Filonov, A.Ye, 1992. Internal-wave trains above the Mascarene Ridge. Atmos. Ocean Phys. 28 (6), 473–479.
Scorer, R.S., 1949. Theory of waves in the lee of mountains. Q. J. R. Meteorol. Soc. 75 (323), 41–56. http://dx.doi.org/10.1002/qj.49707532308.
Scotti, A., Beardsley, R.C., Butman, B., 2007. Generation and propagation of nonlinear internal waves in Massachusetts Bay. J. Geophys. Res. 112, C10001. http://dx.doi.org/10.1029/2007JC004313.
Scotti, A., Mitran, S., 2008. An approximated method for the solution of elliptic problems in thin domains: application to nonlinear internal waves. Ocean Model. 25, 144–153.
Shaw, P.T., Ko, D.S., Chao, S.Y., 2009. Internal solitary waves induced by flow over a ridge: With applications to the northern South China Sea. J. Geophys. Res. 114, C02019. http://dx.doi.org/10.1029/2008JC005007.
Shroyer, E.L., Moum, J.N., Nash, J.D., 2010. Mode 2 waves on the continental shelf: ephemeral components of the nonlinear internal wave field. J. Geophys. Res. 115, C07001. http://dx.doi.org/10.1029/2009JC005605.
Smith, W.H.F., Sandwell, D.T., 1997. Global sea floor topography from satellite altimetry and ship depth soundings. Science 277 (5334), 1956–1962. http://dx.doi.org/10.1126/science.277.5334.1956.
Smyth, W.D., Moum, J.N., Nash, J.D., 2011. Narrowband oscillations in the upper equatorial ocean. Part II: properties of shear instabilities. J. Phys. Oceanogr. 41 (3), 412–428. http://dx.doi.org/10.1175/2010JPO4451.1.
Stashchuk, N., Vlasenko, V., 2007. Numerical modelling of stratified tidal flow over a fjord. Ocean Dyn. 57, 325–338. http://dx.doi.org/10.1007/s10236-007-0112-7.
Thorpe, S.A., 1977. Turbulence and mixing in a Scottish loch. Phil. Trans. R. Soc. Lond. A 286, 125–181.
Valente, A.S., da Silva, J.C.B., 2009. On the observability of the fortnightly cycle of the Tagus estuary turbid plume using MODIS ocean colour images. J. Mar. Syst. 75, 131–137.
Vitousek, S., Fringer, O.B., 2011. Physical vs. numerical dispersion in nonhydrostatic ocean modeling. Ocean Model. 40, 72–86. http://dx.doi.org/10.1016/j.ocemod.2011.07.002.
Vlasenko, V., Stashchuk, N., Guo, C., Chen, X., 2010. Multimodal structure of baroclinic tides in the South China Sea. Nonlinear Process. Geophys. 17, 529–543. http://dx.doi.org/10.5194/npg-17-529-2010.
Vlasenko, V., Stashchuk, N., Palmer, M.R., Inall, M.E., 2013. Generation of baroclinic tides over an isolated underwater bank. J. Geophys. Res. Oceans 118, 4395––4408. http://dx.doi.org/10.1002/jgrc.20304.
Wunsch, S., Ku, H., Delwiche, I., Awadallah, R., 2014. Simulations of nonlinear harmonic generation by an internal wave beam incident on a pycnocline. Nonlinear Processes Geophys. 21, 855–868. http://dx.doi.org/10.5194/npg-21-855-2014.
Yang, Y.J., Fang, Y.C., Chang, M.H., Ramp, S.R., Kao, C.C., Tang, T.Y., 2009. Observations of second baroclinic mode internal solitary waves on the continental slope of the northern South China Sea. J. Geophys. Res. 114, C10003. http://dx.doi.org/10.1029/2009JC005318.